



UNIVERSITY OF AMSTERDAM

MSc Physics

Advanced Matter and Energy Physics

Master Thesis

Polarization- and Angle-Resolved Cathodoluminescence Imaging Spectroscopy of Resonant Optical Nanostructures

by

Philip Heringlake

Stud.Nr.: 10850422

July 2016

60 ECTS

September 2015 - July 2016

1st Examiner:

Prof. Albert Polman

2nd Examiner:

Prof. Tom Gregorkiewicz

1st Supervisor:

Dr. Benjamin Brenny

2nd and 3rd Supervisor:

Dr. Mark Knight

Dr. Sophie Meuret



Abstract

Dielectric resonators at the nanoscale are of increasing importance for novel light managing techniques. Such resonant structures can exhibit complex interactions with light, controlling the wavelength, momentum and polarization of emission. Resolving all these three degrees of freedom at the nanoscale is not feasible for optical excitation techniques due to the intrinsic diffraction limit. Here we apply cathodoluminescence imaging polarimetry, which uses an electron beam as excitation source, to achieve subwavelength spatial resolution. The characterization of the emission from nanoscale silicon disc resonators by spatially and angularly resolved spectroscopic polarimetry enables us to filter the non-polarized incoherent background. By comparing the results to the calculated emission of eigenmodes in these resonators, we can identify characteristics of electric and magnetic modes in resonators of different size. This knowledge is important for dielectric nanophotonic designs based on the precisely tailored coupling between multiple resonators.

Contents

1	Introduction	1
1.1	Dielectric Nanostructures	1
1.2	Measurements at the Nanoscale	2
2	Cathodoluminescence Polarimetry	5
2.1	The Cathodoluminescence Setup	5
2.2	Polarimetry	7
3	Silicon Mie Resonators on a Silicon Oxide Substrate	10
3.1	Fabrication	10
3.2	Theoretical Spectral Response	12
3.3	Cathodoluminescence Measurements	14
3.3.1	Evaluation of the Background Radiation	17
3.3.2	Polarimetry Measurements	19
4	Silicon Mie Resonators on Silicon Nitride Substrate	23
4.1	Fabrication	23
4.2	Cathodoluminescence Measurements	25
4.2.1	Evaluation of Background Signal	25
4.2.2	Polarimetry Measurements	26
4.3	Eigenmode Simulations	32
5	Conclusions	36
	Bibliography	39
	Appendix	42

1 Introduction

Light manipulating nanostructures have recently become an important focus of optical research, opening new fields of applications such as metasurfaces, optical antennas^[1,2] and nanophotovoltaics^[3,4]. Understanding and developing such nanostructures requires high resolution characterization techniques. Cathodoluminescence (CL) imaging nanoscopy is one of these techniques, combining the advantages of electron microscopy and optical measurements. In this research, optical polarimetry measurements on CL are presented as a method to fully characterize the optical response of dielectric nanoresonators.

1.1 Dielectric Nanostructures

Nanosized particles are smaller than the wavelength of visible light, inducing completely different interactions from those between bulk objects and light. In contrast to bulk materials, determined only by material parameters, the geometry of nanoparticles is a key parameter determining the interaction with light, along with their wavelength dependent dielectric response $\epsilon_r(\lambda)$. Due to their small size about a wavelength, the dipolar electromagnetic field of light can drive optical resonances in nanostructures. These resonances often induce an increased local density of optical states in the vicinity of the nanoparticle, leading to enhanced scattering cross sections much larger than the physical cross sections. Since the resonances in nanoparticles can be described by Mie theory, they are called Mie resonances or Mie modes and scattering of these modes is referred to as Mie scattering. Originally, Mie theory has been applied to metal nanospheres, but it also holds for dielectric nanoparticles, characterized by significantly lower losses in the optical frequency regime. These so called Mie resonators are the subject of this research.

Beside the enlarged interaction cross section, dielectric nanoresonators can have a magnetic moment different from one due to the response of some modes to both electric and magnetic fields. These modes are magnetic in nature and based on the induced magnetic moment of one or more current loops within the structure. Electric modes are created by linearly oscillating displacement charges in the resonator, inducing magnetic loops. [Figure 1.1](#) shows the three modes of a cylindrical resonator which are expected to be most relevant for this study ^[5]: an electric dipole mode in (a), a magnetic dipole mode in (b) and a magnetic quadrupole mode in (c). Note that due to symmetry the threefold degeneracy of the cylinder is broken in one dimension such that the presented modes can exist at two different frequencies

with 90° rotation respective to each other. Despite the well-known theory, the

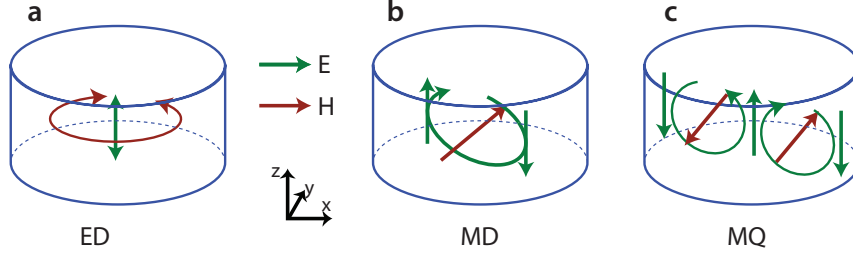


Figure 1.1: The electric dipole ED (a), magnetic dipole MD (b) and magnetic quadrupole MQ mode (c). (a) shows the electrical dipole as oscillating displacement charge (ED, green arrow) and the induced magnetic field loop (red loop). In (b) an circulating current (green loop) induces a magnetic dipole (MD, red arrow). The green arrows indicate the vertical electrical field components of the current loop. In (c) two current loops (green) induce a magnetic quadrupole (MQ, 2 red arrows). The orientation of the presented modes matches those most efficiently measured by CL.

experimental characterization of nanostructures and their intrinsic resonances is of major importance to obtain full control over new designs of resonant structures at the nanoscale. As a model geometry, cylindrical high index resonators made from silicon on a low index substrate will be investigated in this study.

1.2 Measurements at the Nanoscale

Multiple optical measurement techniques are used to investigate nanoparticles. However, most of them are limited by the Abbe diffraction limit and cannot resolve structures smaller than $\lambda/2$ [6]. Thus it is not possible to look at well-defined positions on a nanostructure. Common transmission and reflection measurements only probe an effective bulk medium by measuring a large amount of nanoparticles in an array. One approach to circumvent this limitation is near-field probe microscopy, which brings a nanometer scale probe into the near-field regime of the sample for excitation and detection [7]. The perturbation of the system by the probe is a major disadvantage of this approach together with the impossibility to measure the far-field emission of the resonator. Here, polarization- and angle-resolved cathodoluminescence imaging spectroscopy is applied to investigate the far-field radiation from resonant nanostructures with nanometer spatial resolution. Cathodoluminescence is radiation which is emitted upon the polarization of matter by swift electrons. Electron microscopes provide the ideal platform for creating and measuring cathodoluminescence.

Scanning electron microscopy uses an electron-beam of high energy (100 eV to 30 keV) to image features which are below the diffraction limit of light and thus cannot be resolved by any optical means. Electron microscopes are capable of this imaging since the de Broglie wavelength of an electron is much smaller than the wavelength

of light ^[8], hence the diffraction limit for a 30 keV electron becomes only about 7.1 pm. In reality this limit is not reached because amongst others the electron optics restrict the resolution. The most common method for electron imaging is to collect secondary (SE) and back scattered electrons (BSE), the former created by inelastic collisions within the sample, the latter deflected back by collisions with the nuclei of the material. Since the spot size of the electron beam is of the order of a few nanometers, those signals are sensitive to nanometer scale variations of the investigated structure. Cathodoluminescence imaging microscopy draws a bridge between electron microscopy and optical measurements, as it combines the advantages of the highly spatially confined electron beam with the flexibility of optical measurements. Describing the underlying mechanisms of CL precisely pertains to a whole field of theoretical research ^[9] since the interaction between a single electron and matter happens at the boundary between electrodynamics and quantum mechanics. For a simplified description, the electron beam is regarded as series of single moving point charges. When a charge encounters the sample, the local observer measures a single electric field oscillation as the electron approaches, passes the interface and moves away again. This event is short in time, and hence broad in frequency space. Thus, for a short time, a broad range of frequencies covering the full visible spectrum is present in the sample and can couple to available optical states. This coupling happens preferentially if the field polarization supported by the optical state is parallel to the electron trajectory ^[5].

In this study, dielectric resonators on insulating substrates are subject to cathodoluminescence measurements. The optical processes in these structures are the modes of the dielectric resonators on one hand and electron-hole pair creation and recombination on the other. Radiation from resonant modes can be described as coherent since the direction, phase and polarization of the emitted light are determined only by the mode which is excited by direct electromagnetic coupling to the electric field of the electron. Radiation from recombination centers originates from transitions between quantum-mechanical states and has a random direction, phase and polarization. Thus, luminescence from interband transitions or excited defect states is incoherent. [Figure 1.2a](#) shows a sketch of secondary/back-scattered electron emission and light emission when the electron beam encounters the sample. [Figure 1.2b](#) sketches examples of the directionality of the emission with incoherent radiation having a Lambertian emission profile only determined by Snellius's law of refraction (green dashed line) and coherent radiation emitting in two lobes towards larger angles (red and blue lines).

In the measurement, the emission from resonant modes is detected and its wavelength, directionality and polarization are determined. Since the unique field distribution for each mode of a resonant particle results in a distinct emission pattern, measuring these parameters allows one to identify the excited modes. [Figure 1.2b,c](#) shows the angular emission of a possible dielectric mode in the investigated disc resonators. Here an angle of $\theta = 0^\circ$ corresponds to emission normal to the substrate. The symmetry in [Figure 1.2c](#) results from the circular shape of the disc resonator. However, due to the presence of the substrate and the large penetration depth of the electron beam of

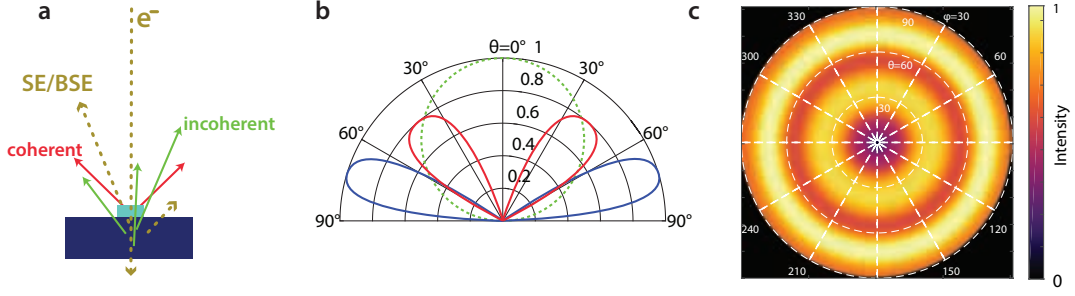


Figure 1.2: (a) Schematic sketch of the signal created by an incident electron beam. Shown are secondary (SE) and back-scattered electrons (BSE) as well as coherent radiation (red arrows) from the sample (bright blue rectangle) and incoherent radiation (green) from electron-hole recombination in the substrate. (b) Polar plot of incoherent radiation (green dashed line), which has a Lambertian emission pattern and coherent radiation (red and blue lines), emitting into lobes at certain angles. (c) Corresponding 2D angular emission pattern similar to that measured with the CL system. The center represents emission normal to the substrate.

several micrometers, a significant part of the detected CL signal is expected to originate from incoherent electron-hole pair recombination at defects in the substrate. This is one motivation for applying optical polarimetry, which is a measurement technique capable of discriminating between different polarization states and determining orientation, ellipticity and handedness of the electric field components. Additionally, the degrees of polarized and unpolarized light can be measured. Thus, in applying optical polarimetry, the incoherent background signal can be filtered from the coherent radiation emitted by resonant modes. Combining polarization resolved measurements of these far-field emission patterns with spectral analysis of the cathodoluminescence signal from multiple nanometer-sized locations on the sample provides all necessary information to characterize the modes of a nanoscale resonator.

In the course of this thesis, the experimental setup is discussed in [Chapter 2](#), followed by a description of polarimetry measurements and its interpretations. [Chapter 3](#) covers the investigation of dielectric modes in cylindrical disc resonators made from silicon on a silicon oxide substrate. Fabrication, simulated and measured results are presented here. Due to an unexpectedly significant perturbation from recombination luminescence at defects in the silicon oxide substrate, a second sample design based on silicon resonators on a silicon nitride layer is realized ([Chapter 4](#)). Its fabrication and the experimental outcome is discussed in chapter four. Finally, [Chapter 5](#) draws conclusions from this research by outlining the unique achievements of the study and discussing the possibilities offered by the technique.

2 Cathodoluminescence Polarimetry

The combination of nanometer resolution electron microscopy with tunable optical measurements allows to characterize the interaction of light with nanophotonic structures. Here, the light's wavelength, propagation direction and polarization are measured as a function of the excitation position of the electron beam. The available CL setup has been specially developed for nanophotonic studies ^[10,11], which require a high detection efficiency and is subject of continuous improvement ^[12,13]. In this section, the different measurement configurations are introduced and subsequently, the important role of polarimetry is discussed.

2.1 The Cathodoluminescence Setup

All described measurements were performed in a FEI XL30 field emission gun (FEG) scanning electron microscope. Luminescence from the sample is collected by a paraboloidal mirror, mounted on a piezoelectrically movable stage to ensure correct alignment of the mirror relative to the sample in the focus of the parabola and the optical setup. The electron beam hits the sample after passing through a 600 μm hole in the mirror presented in [Figure 2.1a,b](#). Due to the small size of the emission

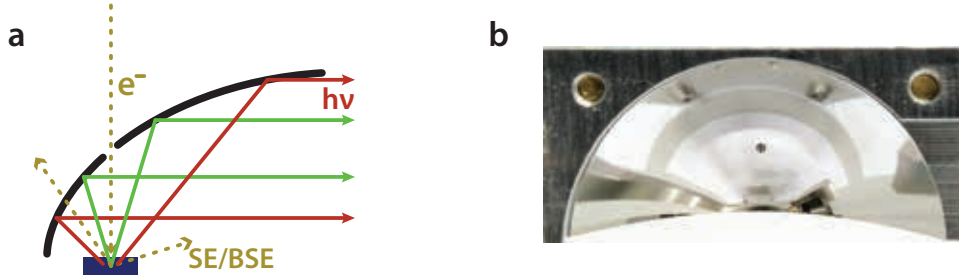


Figure 2.1: **a)** Sketch of the side view into the mirror (black curve). The electron beam (dotted line) passes through the hole and hits the sample (blue rectangle) where it induces the emission of secondary and back scattered electrons indicated by two dotted lines with arrows away from the sample. Additionally the electron beam stimulates emission of cathodoluminescence (red and green lines), which is reflected into a parallel beam by the paraboloidal mirror. **b)** Photograph taken from the mirror's front. The hole is visible in the center of the image.

region being on the order of one wavelength (100 nm to 1 μm) for most nanophotonic

structures, it can be considered an optical point source which emits radiation in the form of spherical waves. The paraboloidal mirror subsequently reflects this spherical wave as a parallel beam with the diameter of the mirror opening. After being reflected, the light is free-space coupled to an optical setup through a quartz window in the vacuum chamber wall. [Figure 2.2](#) gives an overview of the optical elements in the experiment, which is assembled in an opaque black-box to protect the measurement from ambient light.

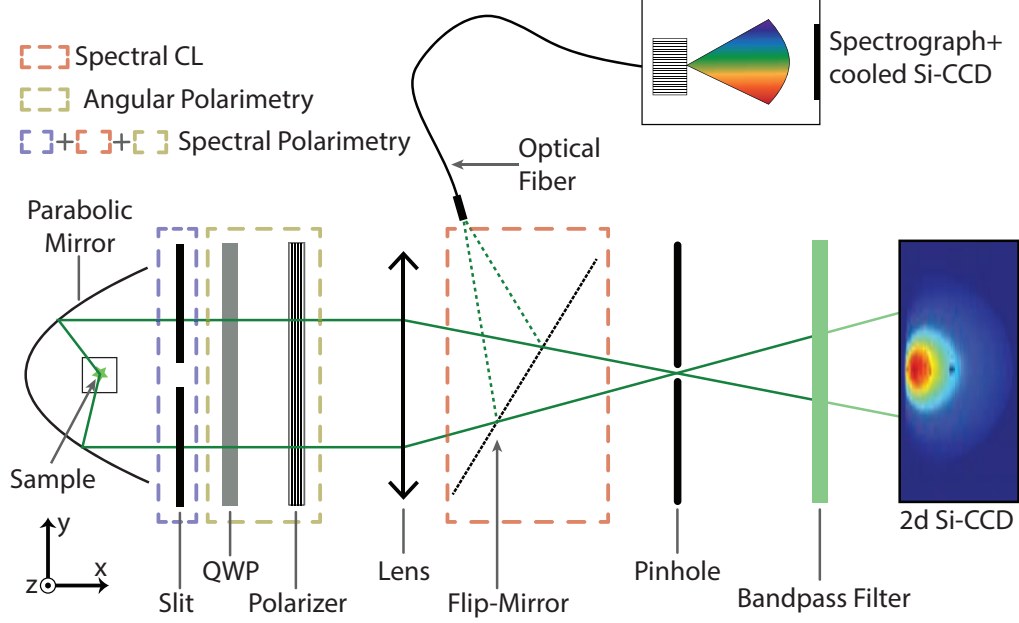


Figure 2.2: The optical setup for CL measurements (top view). Light emitted from the sample is reflected in a parallel beam. For purely **angle resolved CL** measurements all elements within the dashed rectangles are retracted from the beam path. The lens images the mirror's front view onto a 2D Si-CCD camera. The bandpass filter allows for selection of a certain wavelength of the emitted light. For filtering parasitic reflections a pinhole is positioned at the focal spot of the lens. For **spectrally resolved CL**, a flip mirror (red dashed box) reflects the focused light onto an optical fibre which is connected to a spectrometer with a liquid-nitrogen-cooled CCD camera. **Polarimetry** measurements require the insertion of a quarter wave plate (QWP) and a linear polarizer (olive dashed box) in the beam path to select a certain polarization state. A slit (purple dashed box) is added for spectral polarimetry measurements in order to select only the central part of the mirror where the mirror is not curved azimuthally (ϕ close to 0°).

For the basic CL measurements without polarization analysis, the first element encountered by the reflected light is a lens focusing the light either onto an optical fiber via a flip-mirror or imaging the mirror's front view onto a cooled 2D *PIXIS*-CCD camera. Since each angle of emission (θ, ϕ) translates into a unique point (x, y) in the beam cross section projected on the 2D-CCD, each pixel of the camera can be translated to a certain emission angle and the angular emission pattern can be

calculated from that data. To gain an insight into the spectral dependence of the angular emission, a bandpass filter is inserted in the beam path. The selection of available filters covers the range from 400 to 900 nm in 50 nm steps, each with 40 nm bandwidth. Since the optical elements also cause parasitic reflections, a pinhole in the focus of the lens is used to block most of it by filtering in k -space. During angular measurements, the position of the electron beam is fixed by the experimenter.

By focusing the radiation onto the optical using the flip-mirror after the lens (red dashed box in Figure 2.2), the light is guided into a spectrograph with a set of three different adjustable gratings and subsequently detected by a liquid-nitrogen-cooled CCD camera. Thus, for each beam position a full spectrum is acquired for spatially resolved CL measurements.

In order to perform polarimetry measurements, a quarter-wave plate (QWP) and a linear polarizer are added to the setup, allowing the individual measurement of any projection of the polarization state. By choosing the right angles of the QWP and polarizer the projections on six polarization configurations (vertical, horizontal, $\pm 45^\circ$, left/right circular) comprising the full information about the polarization of the emitted radiation are measured. Due to the different angles of incidence at distinct points on the paraboloidal mirror, s- and p-polarized light will be reflected differently caused by the angle dependent Fresnel coefficients. By using a complete Mueller matrix formalism, these geometrical polarization transformations on the mirror can be corrected for angular measurements. In case of spectrally and spatially resolved polarimetry, all light emitted into different angles is collected by the optical fiber which makes it impossible to apply the correction routine since all information about the location on the mirror from where the light is reflected is lost. Hence, a slit is used to filter out the central part of the mirror, which is approximately flat in the horizontal direction, meaning that it has the least influence on the emission's polarization. However, it covers part of the reflected light and decreases the total collection efficiency. A slit width of 3 mm has proven to induce only small losses since the solid angle of the mirror is largest for the central part not covered by the slit, and at the same time only reduces the polarization contrast slightly^[14].

2.2 Polarimetry

In order to retrieve the full polarization information from the emitted light, which consists of three orthogonal parameters, the intensities of six different polarizations need to be measured experimentally. These are vertical (*ver*), horizontal (*hor*), $\pm 45^\circ$ and left/right handed circularly (*LHC*, *RHC*) polarized. Together with a reference measurement for the total emitted intensity (*tot*) obtained without QWP and polarizer, this results in the following set of intensity measurements:

$$I_{tot}, I_{ver}, I_{hor}, I_{+45}, I_{-45}, I_{LHC}, I_{RHC}$$

A convenient way for describing the polarization state of light is the four element Stokes vector \mathbf{S} with

$$S_0 = I_{tot} = I_{hor} + I_{ver} \quad (2.1)$$

$$S_1 = I_{hor} - I_{ver} \quad (2.2)$$

$$S_2 = I_{+45^\circ} - I_{-45^\circ} \quad (2.3)$$

$$S_3 = I_{RHC} - I_{LHC} . \quad (2.4)$$

For fixed intensity I_{tot} all possible polarizations \mathbf{S} lie on a sphere with radius S_0 and S_1, S_2, S_3 as orthogonal base vectors. Normalizing \mathbf{S} by the total intensity puts all polarization states into a sphere with radius one, the so called Poincaré sphere which is presented in [Figure 2.3](#). The normalized stokes vector is described by

$$\mathbf{S}' = (S_1/S_0, S_2/S_0, S_3/S_0). \quad (2.5)$$

A possible measurement outcome \mathbf{S}' is shown as a blue arrow with a length varying from 0 (completely unpolarized) to 1 (fully polarized), called degree of polarization *DOP*. Most modes in the investigated dielectric disc resonators are expected to emit linearly polarized light as emitted by electric and magnetic dipole and quadrupole modes. Thus, it is beneficial to separate \mathbf{S}' into a linearly and circularly polarized part (green and orange arrow respectively in [Figure 2.3](#)). The length of these vectors is called degree of linear/circular polarization (*DOLP/DOCP*) following the convention

$$DOP = \frac{\sqrt{S_1^2 + S_2^2 + S_3^2}}{S_0} \quad (2.6)$$

$$DOLP = \frac{\sqrt{S_1^2 + S_2^2}}{S_0} \quad (2.7)$$

$$DOCP = \frac{S_3}{S_0} \quad (2.8)$$

$$DOUP = 1 - DOP , \quad (2.9)$$

where *DOUP* is the degree of unpolarized light.

In the analysis of a measurement, splitting the measured polarization into a polarized and unpolarized part is expected to reduce the incoherent background signal from defect states and interband transitions in the substrate emitting primarily unpolarized light. Separating the linearly and circularly polarized fraction allows to distinguish and identify dielectric modes in spectrally and angularly resolved CL measurements. Furthermore, the knowledge of the polarization of the light allows for calculation of the orthogonal electric field components E_h and E_v respectively, and their phase relation Δ . The field amplitudes and the relative phase of the polarized light can be

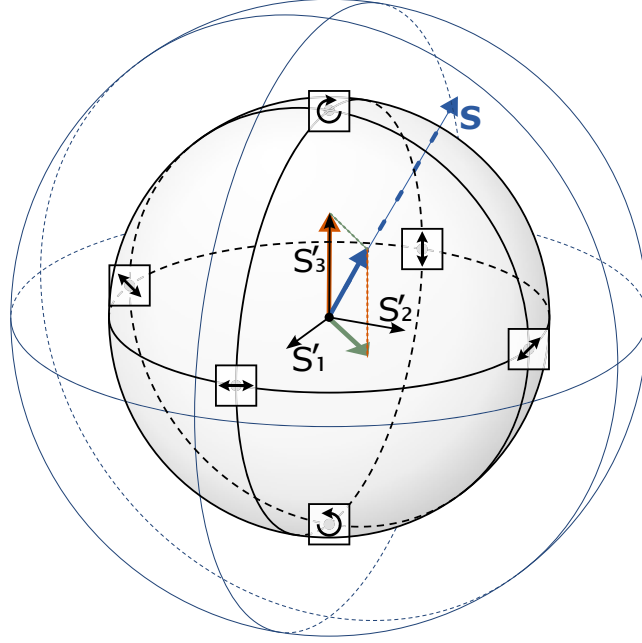


Figure 2.3: The Poincaré sphere (inner sphere) and the sphere on which the unnormalized Stokes vector \mathbf{S} lives (outer sphere). The latter sphere has the radius S_0 , the Poincaré sphere itself radius one. The intersections with the coordinate axes represent each a state of fully linearly or circularly polarized light on the equator plane, respectively the poles. All other points on the sphere represent elliptically polarized light. An unnormalized \mathbf{S} is drawn as blue dashed line, its normalized representation is the blue arrow which can be decomposed into the components S'_1, S'_2, S'_3 . The projections of this normalized state on the equator plane (green arrow) and the rotation axis (orange arrow) are then the linearly and circularly polarized parts. The length of the colored vectors is called degree of (linear/circular) polarization.

determined by

$$\|E_h\| = \sqrt{\frac{S_0 \times DOP + S_1}{2}} \quad (2.10)$$

$$\|E_v\| = \sqrt{\frac{S_0 \times DOP - S_1}{2}} \quad (2.11)$$

$$\Delta = \arctan\left(\frac{S_3}{S_2}\right) \quad (2.12)$$

where $S_0 \times DOP$ is the intensity of the polarized light. Note that in the experiment this entity suffers from parasitic absorption in the QWP and polarizer. This needs to be considered for an absolute quantitative interpretation. However, the absorption in the optical elements is a systematic error which does not influence the measurement results presented in this thesis.

3 Silicon Mie Resonators on a Silicon Oxide Substrate

The investigated structures are cylindrical silicon disc resonators on an insulating substrate. The sample geometry is a 100 nm thick Si device layer on a 300 nm thick SiO₂ layer on top of a Si handle wafer. The combination of a high refractive index of the Si in the device layer and the lower index of the SiO₂ substrate reduces the coupling efficiency between resonators and substrate leading to a decrease of the optical loss and an enhancement of the resonator quality. Thanks to good control of the fabrication process a precisely adjusted sample design is possible. After a description of the fabrication process, finite-difference time-domain (FDTD) calculations provide an indication of the expected resonances in the investigated samples, followed by a discussion of the experiment and its results.

3.1 Fabrication

Cylindrical resonators of different sizes are fabricated on a Si-SiO₂-Si wafer with a 100 nm single crystalline Si device layer on a 300 nm silica layer. The fabrication procedure is sketched in [Figure 3.1](#). First, the substrate is cleaned in acetone, subsequently rinsed with isopropanol (IPA) and ultrasonicated in H₂O for 10 min to remove a protective resist coating from the device layer. Additionally, further residues of organics are removed by a 10 min clean in a mixture of H₂O, NOH₅ and H₂O₂ (5:1:1) at 75°C (base piranha). Subsequently, the sample is dipped twice in H₂O for 15 s, rinsed with IPA and blow-dried with nitrogen. To remove condensed water from the sample, it is heated on a hotplate at 110°C. After cooling with nitrogen, between 50 nm and 60 nm of the electron-beam lithography (EBL) resist hydrogen silsesquioxane (HSQ) (1:2 diluted with methylisobutylketon (MIBK)) are spincoated at 4000 rpm (revolutions per minute) for 45 s with an acceleration of 1500 rpm/s. Next, the resist is baked for 2 min at 180°C. A solution with Au nanoparticles is dropcast in the sample corner and baked for one more minute at 180°C in order to achieve a better alignment in the EBL system. A *Raith e-LINE* system is used to write the desired structures in the HSQ resist with a 10 µm aperture and 30 keV beam current. Best results were achieved with doses between 1 mAs/cm² and 1.2 mAs/cm² in area exposure mode. Next, the exposed resist is developed in MF-319 *Microposit* developer for 70 s at 50°C. To stop the development, the sample is rinsed twice in deionized H₂O for 15 s each. Since the sample could not be etched immediately after the lithography step, it is cleaned before the etching by 10 min ultrasonication in

water and subsequent rinse in IPA to remove dust particles. The reactive ion etching (RIE) step is performed at 60°C in an *Oxford PlasmaPro 100 Cobra* device with a short (15 s) Cl_2 based etch (7 mTorr base pressure, 30 W forward power, 750 W ICP power, 50 sccm Cl_2 flow) to remove native oxide from the silicon followed by the main HBr/O_2 based Si etch (7 mTorr base pressure, 30 W forward power, 750 W ICP power, 48 sccm HBr flow, 2 sccm O_2 flow) for a duration of 60 s. The fabrication process is completed with a 3 min dip in 1% hydrofluoric acid (diluted with H_2O) and a subsequent rinse in water. Figure 3.2 shows a secondary electron (SEM) image for

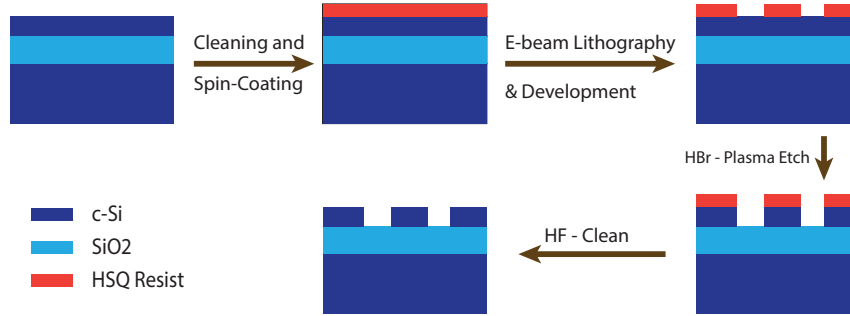


Figure 3.1: The fabrication workflow, showing the sample in the most important intermediate states after cleaning and spin-coating, after lithography, etching and finally after the HF clean.

one of the measured Mie resonators (a) and a focused ion beam (FIB) cross section of another resonator of the same size. The resulting Mie resonators are of good circular shape and have a wall angle of 86° to 88°. Secondary electron images on whole structures and FIB cross sections as well as AFM measurements show different resonator heights. On average, a height of (120 ± 10) nm can be measured. This difference with the expected height can be explained by spatial deviations of the device layer thickness as well as by an etch of the silica substrate during the HF clean, increasing the effective resonator height. Besides the bare silica substrate, large pads of silicon with micrometer-sized dimensions act as reference for later CL measurements to provide information about possible radiation from the silicon layer and the influence of the thin high index material.

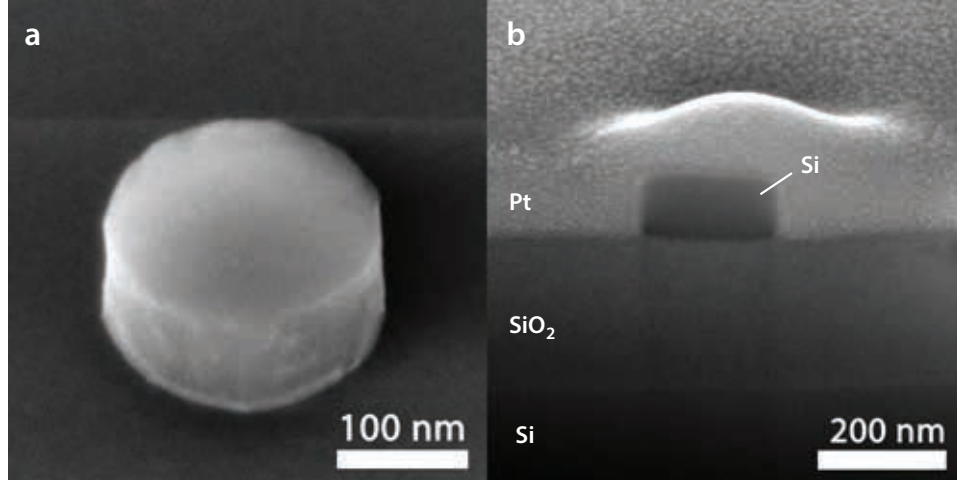


Figure 3.2: (a) SEM image of a resonator taken under a tilt of 45°. The circular shape of the resonator as well as its uniform flat walls are clearly visible. (b) Focused ion beam cross section of a resonator with same dimensions. The bright grainy top layer is platinum, deposited to protect the surface from the ion beam. The wall angle of the resonators lies between 86° and 88°. Beneath the resonator, the substrate layout with 300 nm of silica and the silicon handle layer is recognizable.

3.2 Theoretical Spectral Response

Finite-difference time-domain (FDTD) calculations are performed using the *Lumerical* software to simulate the coupling between dipole excitation and dielectric modes in cylindrical disc resonators, matching the geometries of the measured ones. The calculated emission indicates the expected resonance wavelengths of the dielectric modes. A broadband z -oriented dipole source in the resonator is used to model the excitation with an electron-beam. This approach originates from the similarity between the incident electron and its induced image charge, and a dipole. A more sophisticated source design consisting of multiple dipoles along the trajectory [15], each with a different time delay, has not proven to lead to very different results in this study [5,16]. Hence, a good qualitative representation of the electron-beam by a dipole source is assumed for the performed simulations. Figure 3.3 displays the simulation geometry with the silicon resonator in the central region and the dipole source within the resonator. For detection of the emitted light, a transmission monitor is placed above the resonator to collect all light vertically propagating. Convergence tests were performed to optimize the simulation, which uses a non-uniform mesh with maximum mesh steps of 5 nm to discretize the geometry. The calculation results for eight resonator diameters are presented in Figure 3.4. For each diameter two simulations are performed, once with the source being located in the center of the particle and once close to its edge (dashed lines) in order to probe various modes with dissimilar spatial field profiles and thus different coupling probability depending on



Figure 3.3: Geometry of the 3d FDTD simulations (cross-cut) as it is implemented in *Lumerical*. The resonator is located on top of the silica layer in the center of the image. The blue arrows indicate the position of the dipole source for this specific simulation. The transmission monitor (yellow line) is placed above the resonator, sticking through the perfectly matched layers (orange).

the excitation location. In the spectra for smaller diameters from 155 nm to 238 nm some peaks are only present at central or edge excitation. This is due to the intrinsic field profile of different modes. For instance in Figure 3.4a, the peaks (emphasized by vertical dashed lines) for excitation at the edges at 600 nm (red dashed curve) and 650 nm (blue dashed curve) suggest a magnetic dipole mode with large z-component of the electric field close to the resonator edges and none in the center. Thus, the z-dipole source can only couple to this mode off-center. Other modes, for instance the central pair of peaks in plots Figure 3.4a,b can be excited at both positions, whereas the peaks at smallest wavelength are only present under central excitation. For increasing diameters, a red shift of the peaks can be observed while higher orders enter the spectrum at short wavelength. As more modes appear, the correlation between peaks and excitation position becomes less well defined since the field profile for higher order modes is more complicated than for dipole modes. Especially for the largest resonators in Figure 3.4d, the modes of central and edge excitation are close together, making it difficult to measure them independently from each other. Note that the peaks' height does not necessarily provide information about the measured CL intensity since excitation by an electron-beam is different from the simulated source due to the fact that it moves through the material and thus represents only one field oscillation at all points on the trajectory whereas the FDTD dipole source can have multiple oscillations but only at a single point. Additionally, the FDTD simulations do not take into account incoherent emission from the substrate, which can couple to the dielectric modes as well.

In the preliminary FDTD simulations, various peaks across the VIS regime (400 nm-700 nm) that shift with resonator size and excitation position can be observed. In the following step, they can be compared to the measurements to determine whether there are consistent similarities or differences.

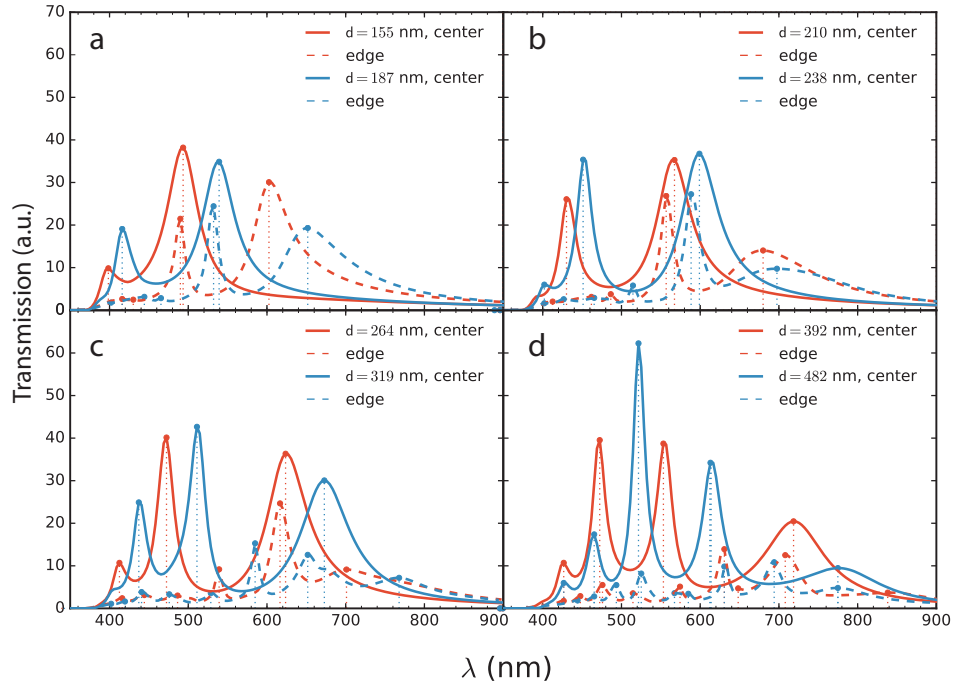


Figure 3.4: The simulated transmission spectra for eight resonators with 155 nm and 187 nm diameter (a), 210 nm and 238 nm diameter (b), 264 nm and 319 nm diameter (c), and 392 nm and 482 nm diameter (d). The dashed curves are results from simulations where the exciting dipole source is placed close to the edge of the particle. Peaks which only show up in the continuous or dashed line result from different field profiles in the resonator. Increasing particle size leads to red-shifting peaks and higher order modes appearing from the blue side of the spectrum.

3.3 Cathodoluminescence Measurements

The first wavelength resolved CL scans for multiple resonators were performed using a beam voltage of 30 keV at a beam current of about 0.9 nA. A dark reference quantifying the noise signal when the electron-beam is blanked is subtracted from the data and the wavelength-dependent system response is taken into account in the correction. The measured CL maps for a 210 nm diameter Mie resonator are presented in Figure 3.5a,c for 450 nm and 650 nm. Both maps show a strong background from the substrate around the particle, which has a brighter signal due to more efficient scattering to the far-field of light created in or beneath the resonator. The signal from the substrate in Figure 3.5a has a spatial dependence as it changes from top to bottom of the CL map, corresponding to the scan direction of the electron-beam. This behavior can be attributed to the electron-beam induced creation and excitation of defects in the silicon-dioxide layer, matching the peaks in the background spectrum,

and has been investigated extensively in the past [17–19]. The increasing background makes it difficult to correct for it using simple reference spectra. Thus, a background reference is calculated with a triangulation routine, interpolating a smoothly changing background to 16 spots along the edges of the acquisition frame (squares in Figure 3.5a) and subsequently subtracted from the data. The resulting corrected CL maps are presented in (b) and (d) of Figure 3.5. After correction, the intensity distribution of the particle in the 450 nm map is much more symmetric, showing less CL intensity in the particle center than at the edges. A clear feature is observable in the particle center in the CL map at 600 nm together with a bright ring at the particle rim. This matches the simulated peak positions in Figure 3.4-b where central and edge excitation induce transmission at similar wavelengths. The secondary electron images in Figure 3.5e,f display an taken before the measurement (e) and an image taken during the CL measurement (f), having lower resolution. The lines in Figure 3.5f originate from drift during the spatial CL scan.

Next, spectral polarimetry measurements as described in Section 2.2 are performed in order to resolve the spectral position of dielectric modes. For this, it is convenient to plot the wavelength dependent degree of polarization and analyze it with respect to peaks in the polarized parts. Figure 3.6 shows this data averaged over the area of a 210 nm large particle neglecting the surrounding substrate. The QWP wavelength range is 450 nm to 700 nm, thus any data taken from this range needs to be considered with care. First, the high degree of unpolarized light (DOUP) suggests a strong unpolarized background matching the observations from the previous measurements. The degree of linear polarization shows some sharp peaks around 450 nm and a strong peak at 570 nm. At both locations a distinct feature in the degree of circular polarized light can be observed as well. This stands in contrast to the expectations since the targeted modes that are electric and magnetic dipole and quadrupole modes should not emit circularly polarized light, as examined later in Section 4.3. Thus, a flat DOCP curve is anticipated if light is emitted mainly from those resonances. An error source which can induce deviations from this expectation is the background intensity change between polarimetry measurements. This change induces an error which is different for each of the six polarization measurements and translates into wrong Stokes parameters and a wrong degree of (circularly, linearly) polarized light. The position of the peaks in DOLP at the maxima of the background signal is another hint that further investigation of the background is required.

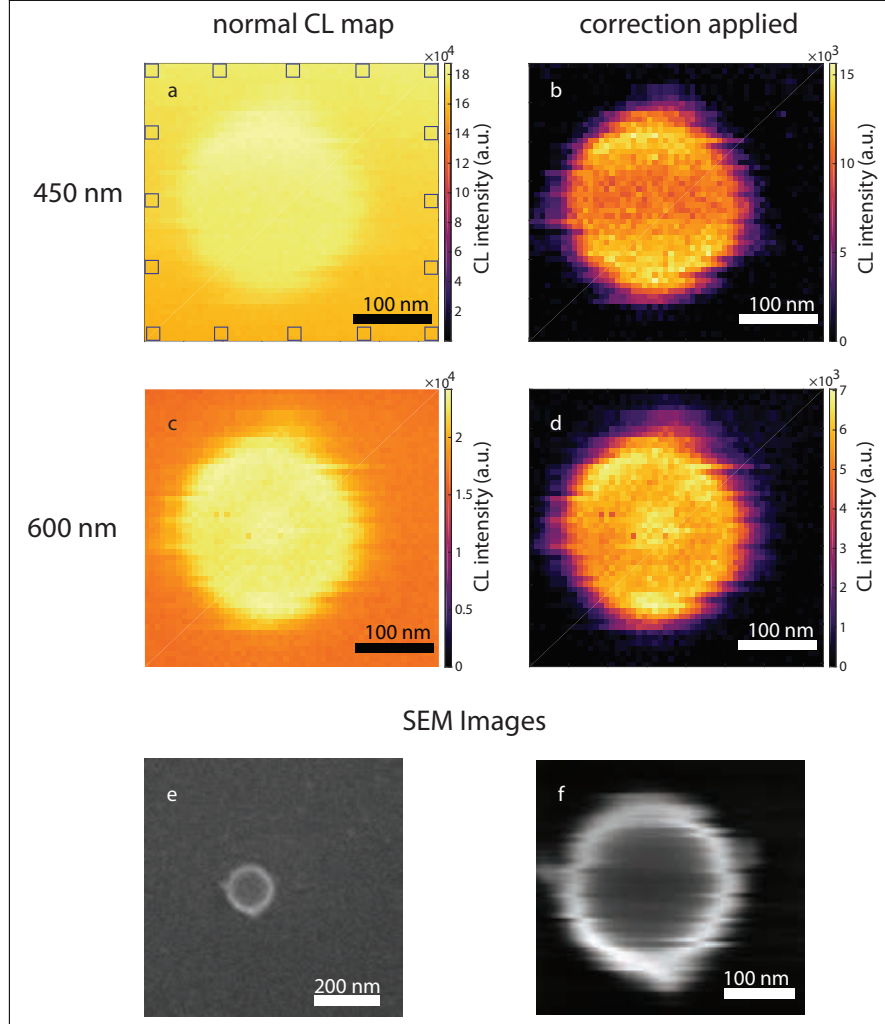


Figure 3.5: Images (a) and (c) present the measured CL intensity at 450 nm and 650 nm, respectively, with applied correction for the dark background and the system response. The colormap scales to the maximum of the according dataset. The squares in (a) indicate the areas which are used to interpolate the background which is consequently subtracted from the data to create the plots in (b) and (d) showing the corrected data. Images (e) and (f) show a survey SEM image acquired previous to the measurement and a SEM image recorded at the same time as the CL experiment respectively. The secondary electrons are more likely to escape from the particle edges, increasing the brightness in the SEM image, comparing the edges to the darker particle centers.

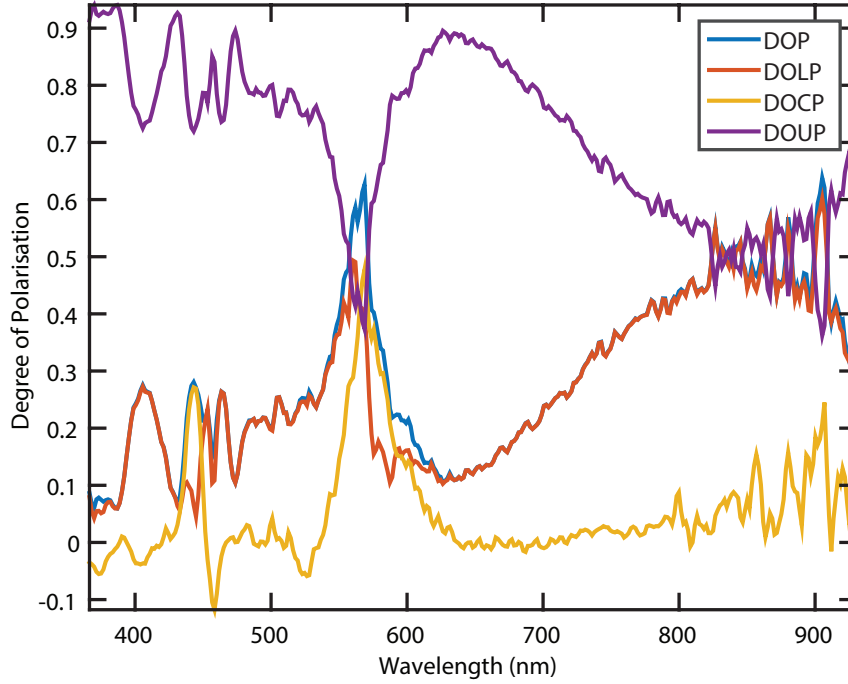


Figure 3.6: The spatially averaged degree of polarization is shown for a 210 nm diameter resonator. As expected, the degree of unpolarized light (DOUP) is high, representing a mainly unpolarized background. Features in the degree of linearly polarized light (DOLP) can hint to dielectric modes in the sample whereas the degree of circularly polarized light (DOCP) is expected to be flat. Note that the DOCP is the only quantity which can be smaller than zero, representing left hand circular polarization.

3.3.1 Evaluation of the Background Radiation

Reference spectra on the silica substrate and on large silicon pads on top of the silica are taken together with a dark reference (Figure 3.7a) to quantize the spectral shape of the background radiation. The dark background (blue) is small and does not show any spectral features. Both reference measurements on silica substrate and silicon pad show a high peak at approximately 460 nm and a smaller peak at 650 nm while the relative change between the measurements of the two peaks is of different sign. Furthermore, the 460 nm peak is significantly higher and sharper in the silicon reference than on the silica substrate, which is attributed to the enclosed low index silica layer, supporting Fabry P  rot modes with influence on the emission's linewidth.

The peaks in Figure 3.7a can be attributed to electron-hole pair recombinations and hence do not emit polarized light. However, due to different reflection coefficients for normal and parallel polarized light at the SiO₂/air interface, a small fraction of less

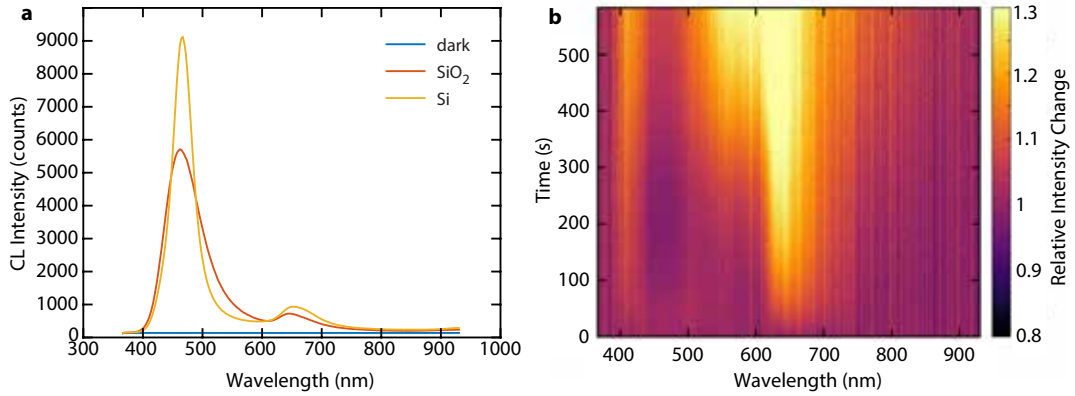


Figure 3.7: (a) The reference spectra averaged over 10 by 10 pixel taken with blanked beam (dark) as well as references from the silica substrate and from a micrometer sized silicon pad. All spectra are not corrected for the system response. The narrower peak in the silicon spectrum can be explained by internal reflections in the silica slab, which lead to Fabry P rot resonances. In image (b) the time dependent relative CL intensity change is presented. The data is normalized to the average of the first four spectra. It can be observed that the signal varies between a decrease of about 5% to an increase of more than 30%. The measurements were conducted under same voltage and beam current as the ones in [Section 3.3](#).

than 10% of the light is expected to be polarized for certain angles of emission. See [Section A.1](#) for the calculation. The Fabry P rot resonances (red curve) leads to polarization of the light, as well. However, due to the small particle sizes compared to the large reference pads, this effect is expected to be minor.

To quantize the change of the background during the measurements we acquire a sequence of spectra while the beam remains positioned at the same spot. The relative intensity change over time is obtained by normalizing the data with a mean of the first four acquired spectra. It is plotted in [Figure 3.7b](#). Most apparently, the signal changes by more than 30% over a broad part of the visible spectral range during a timescale of several minutes. The region of the stronger of the two background peaks from 450 nm to 490 nm only shows a slight decrease in signal during the first three minutes, whereas the peak intensity between 600 nm to 700 nm increases by 20% already in the first minute. The signal between the two peaks rises significantly with advancing time as well. All those changes have been studied in the past and can be matched to about five different types of defect centers ^[17–19]. Measurements after a 20 min to 30 min period of continuous exposure of an area to the electron-beam have shown that the signal from those defect centers stabilizes. A stable background is essential for success of the CL polarimetry routine because it relies on the assumption that the total intensity is the same for each of the six consequent measurements. For the measurements, this means each polarimetry measurement requires a preceding irradiation step in order to reach an equilibrium between defect creation/excitation

and decaying defect centers.

3.3.2 Polarimetry Measurements

The performed polarization resolved cathodoluminescence measurements comprises two steps, which are spectrally resolved polarimetry to identify the position of resonances and subsequent angle-resolved polarimetry to investigate their far-field emission pattern. These steps are discussed in this section.

Spatially Resolved Spectral Polarimetry

By scanning the electron-beam over the selected particle for half an hour previous to the measurements, the variation in substrate background signal can be reduced to an acceptable minimum. Figure 3.8a presents the measured degree of polarization for a Si disc with 240 nm diameter, obtained by averaging the CL spectrum over the whole particle. Again, most of the light is unpolarized which is represented by the high DOUP. In contrast to the previous measurements, the circular part of the DOP is relatively flat and close to zero which matches the expectations. The linearly polarized part (red curve in Figure 3.8a) shows some prominent peaks in the region of interest between 450 nm and 700 nm. Spectral polarimetry was performed on eight

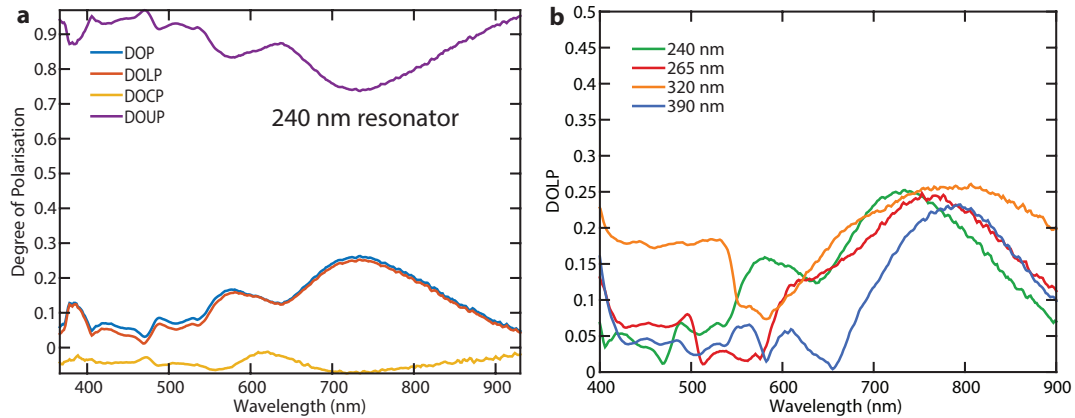


Figure 3.8: (a) The results from spectral CL polarimetry measurements on a 240 nm diameter resonator. To get the displayed spectra we averaged all CL pixels of the resonator, neglecting the surrounding substrate. (b) The different curves show the degree of linearly polarized light for resonators of different diameter. For increasing diameter there seem to be at least two features shifting towards larger wavelengths.

particles of different sizes. For all of them a flat DOCP curve as well as the expected strong and highly unpolarized background was observed. Comparing the differences of the linearly polarized components (Figure 3.8b) indicates that some of the features in the curves are consistent for all presented particles. The first is the broad linearly

polarized part around 700 nm which is present in all measurements and lies at the edge of detection sensitivity. Second is the feature which starts as a peak at 580 nm in the 240 nm resonator and shifts to larger wavelengths becoming a shoulder of the 700 nm feature as particle size increases. A similar behavior is observed for the third feature which peaks at 485 nm, 500 nm, 530 nm and 565 nm, for increasing diameters 240 nm, 265 nm, 320 nm and 390 nm respectively. The fact that the peaks shift as diameter increases can be attributed to particle size dependent resonator modes. This proves that area pre-irradiation of the substrate solves the issue of irradiation dependent background signal from defect radiation in CL measurements. To apply this method in a general way, the measurement's sensitivity to carbon deposition has to be small since the electron irradiation procedure induces carbon deposition on the sample. Possible candidates for more detailed investigation by angular measurements can be identified in [Figure 3.8b](#). These features of interest are determined by the restricted wavelength selection in angular CL measurements. Thus, the peaks at 500 nm and 600 nm for the 265 nm particle and those at 560 nm and 600 nm for the 390 nm particle are promising candidates. This selection is also supported by an analysis of the polarized intensities which are the products of the total emission spectrum S_0 and the different degrees of polarization. These graphs are displayed in [Figure A.2](#).

Angular Polarimetry

Angular polarimetry measurements were performed for resonators of eight different diameters using band-pass filters at 50 nm increments between 400 nm and 700 nm and 40 nm bandwidth, partly with multiple excitation spots on the resonators, resulting in a set of more than 90 full polarimetry measurements, each comprising of seven single measurements (total intensity plus six polarization states). A full overview of the investigated resonators is given in [Table A.1](#). Note that sample destruction and carbon deposition during the measurements required to switch to a new particle of the same dimensions after angular CL polarimetry measurements at approximately four different wavelengths (see [Section A.4](#)). In the following, the 265 nm and 390 nm resonators shall be discussed as examples. As before, the degree of linearly polarized light is the measure which provides most information about the source of radiation and distinct features in the angular DOLP profile allow for reliable identification of different radiating modes by comparison to simulated far-field patterns.

The measured angular DOLP for the selected resonators under central excitation at 500 nm and 600 nm wavelength for the 240 nm large resonator, respectively 550 nm and 600 nm wavelength for the 390 nm large resonator is plotted in [Figure 3.9a,c](#). [Figure 3.9b](#) shows the degree of circularly polarized light for the 240 nm particle and [Figure 3.9d](#) presents the DOLP for the 390 nm resonator with the excitation spot close to the right edge of the particle. The DOCP plot in [Figure 3.9b](#) represents the results for all measured combinations since in none of them the DOCP deviates much from zero, which supports the expectation that no sources of circularly polarized light

are present. The small features in DOCP of a magnitude of less than 0.2 have been observed before ^[20] and can be explained by the mirror's influence on the polarization and non perfect correction for these effects.

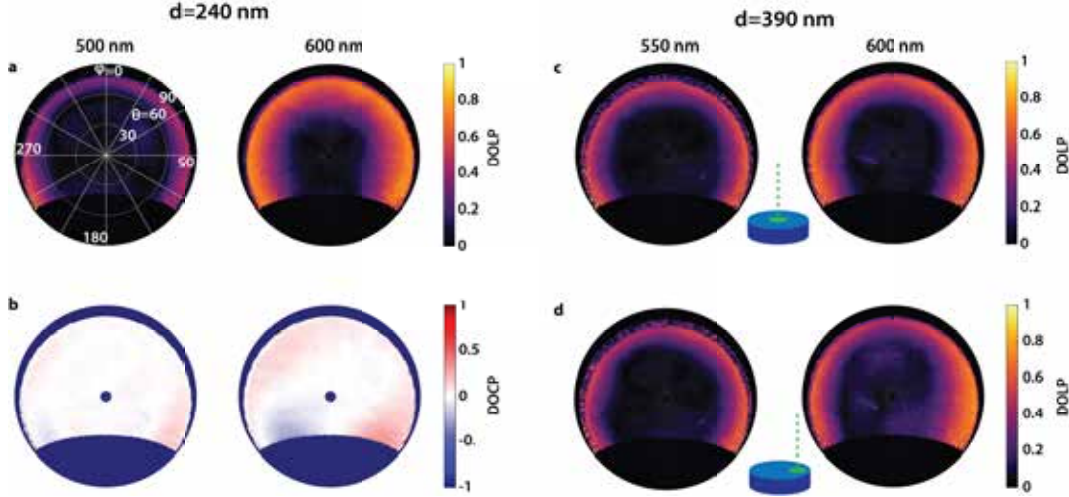


Figure 3.9: Selected results from angular polarimetry measurements on a 240 nm and a 390 nm large resonator. A value $\theta = 0$ means upward emission whereas $\theta \rightarrow 90^\circ$ are grazing angles parallel to the sample surface. ϕ is the azimuthal angle with $\phi = 180^\circ$ as the direction towards the CCD detector. Figures (a) and (b) show the DOLP (the DOCP respectively) at 500 nm and 600 nm wavelength for the smaller resonator. All measured results are similar to the presented DOCP. (c) and (d) plot the DOLP of the larger resonator, which is excited in the center (c) as well as at the right edge (d).

A general behavior observable in all three DOLP plots is the relatively high linearly polarized fraction at large angles θ corresponding to emission nearly parallel to the x,y plane. At the shorter of the chosen wavelengths, this phenomenon is more pronounced than at the longer wavelength. Taking into account the angular profile of the total emitted intensity S_0 slightly alters the amplitudes but does not qualitatively change the observed behavior (see [Section A.2.3](#)). The region with $\theta \rightarrow 90^\circ$ is the area where the least signal is collected since the unpolarized main part of the light is emitted upwards. This can lead to a speckle pattern as observed for 550 nm in [Figure 3.9c](#) and d, if the measured intensity is close to the background level in the measurements determining the DOLP. The higher degree of polarization can either result from the emission of dielectric modes or be related to the small intensity of the unpolarized background which is described by a Lambertian pattern (see [Figure 1.2](#)). Additionally, the silicon oxide/air interface induces a small ratio of polarized light at angles around 60° (see [Section A.1](#)). However, this is a minor effect and does not explain the observed behavior at high angles. As a result of the non-symmetric excitation in [Figure 3.9d](#), the bright features at the right side of the plot are slightly more pronounced than at the left. Furthermore, the emission at 600 nm from the 390 nm large resonator has additional regions of linear polarization at angles between

30° and 60°.

Cathodoluminescence measurements on cylindrical silicon resonators allowed to resolve the spatial mode profiles and their spectral location by analyzing the DOLP. In the angular measurements clearly distinguishable features are required associate angular emission patterns with the nature of the modes. One reason for their absence could be an underestimation of the influence of the background on the measurement. The strong luminescence from the silica layer quickly leads to saturation of the detector so that insufficient radiation from the photonic modes can be collected. Thus, an improved sample design with silicon nitride, known to possess less radiating defects than SiO₂, is investigated in the following section.

4 Silicon Mie Resonators on Silicon Nitride Substrate

In order to achieve a better contrast to resolve the signal from the dielectric photonic modes, reducing the background luminescence seems crucial. In changing the substrate from SiO_2 to Si_3N_4 , a large fraction of defect luminescence can be avoided and hence a smaller and more stable unpolarized background signal is anticipated. After the description of the fabrication process and a discussion of the experimental results from selected resonators, the measurement will be related to theoretical calculations of the dielectric resonances from finite-element eigenfunction studies.

4.1 Fabrication

The transition to another substrate requires an adjusted fabrication procedure since a commercial c-Si on nitride wafer was unavailable. Thus, a single side polished single crystalline silicon wafer, coated with 319 nm of Si_3N_4 by liquid phase chemical vapor deposition (LPCVD) was used as substrate for the fabrication. The thickness of the nitride layer has been determined by an optical ellipsometry measurement, which in addition provides the optical constants of the layer (see [Figure 4.1](#)).

After a 10 min base piranha clean (H_2O , NOH_5 and H_2O_2 (5:1:1)) at 75°C and succeeding rinse in H_2O , a silicon layer is deposited by electron beam induced evaporation at room temperature under a vacuum of 1.9×10^{-6} mbar. Subsequently, the silicon layer was annealed in order to reduce defects and create larger crystalline domains. Different annealing methods were available. Tube-oven annealing under vacuum at 800°C for 1 h resulted in the largest connected Si domains and lead to crystalline silicon resembling ellipsometry results. The thickness of the annealed layer was determined to be 140 nm by ellipsometry measurements and from focused ion beam cross sections. After these preparation steps the same lithography procedure as in [Section 3.1](#) was applied, with the difference that the reactive ion etching time was increased to 90 s. [Figure 4.2](#) sketches the fabrication process.

The resulting resonators are 140 nm high and have different diameters. [Figure 4.3](#) shows the secondary electron image of a 260 nm large particle (a) and the FIB cross section through a 600 nm large resonator (b). The walls are less straight than after the previous fabrication and some residue is present on the Si_3N_4 surface after the etch. It is attributed to nanograin formation in which sputtered material from debris

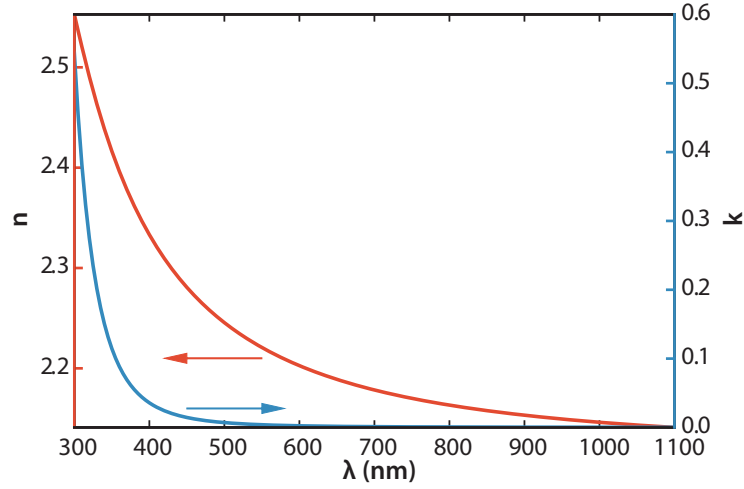


Figure 4.1: The real (n) and imaginary (k) part of the complex refractive index of the LPCVD silicon nitride layer determined by optical ellipsometry.

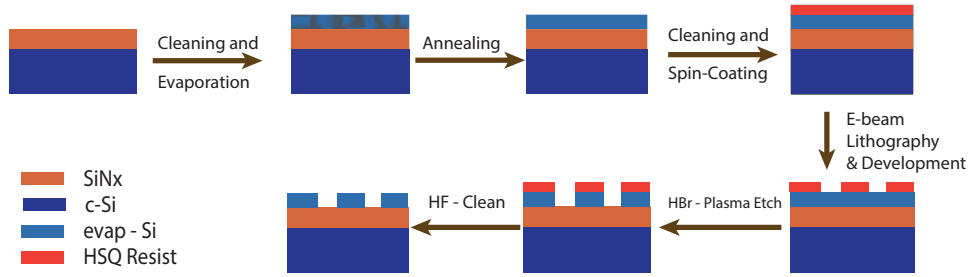


Figure 4.2: Sketch of the fabrication workflow of silicon resonators on Si_3N_4 , showing the sample after the most important steps.

on the sample such as carbon decontaminations redeposits during the etch and acts as a mask for the RIE process. The grains proved resistant against longer etch times and cleaning with 1% HF, which suggests that nitrogen diffused into the evaporated silicon during the annealing step, making some of the silicon resistant against the etches. However, due to their size these particles are not expected to affect the CL emission from the resonator. The observed roughness of the resonator walls is slightly higher than what was found for the previous set of samples based on silicon oxide. The insulating nitride layer is visible as a bright area beneath the resonator in [Figure 4.3-b](#). Despite the reduced geometrical quality, the fabricated particles can still be expected to support the same fundamental modes as a perfect cylindrical resonator. This, together with the limited time frame for this project, motivates the decision to perform CL measurements on the fabricated structures instead of optimizing the fabrication process.

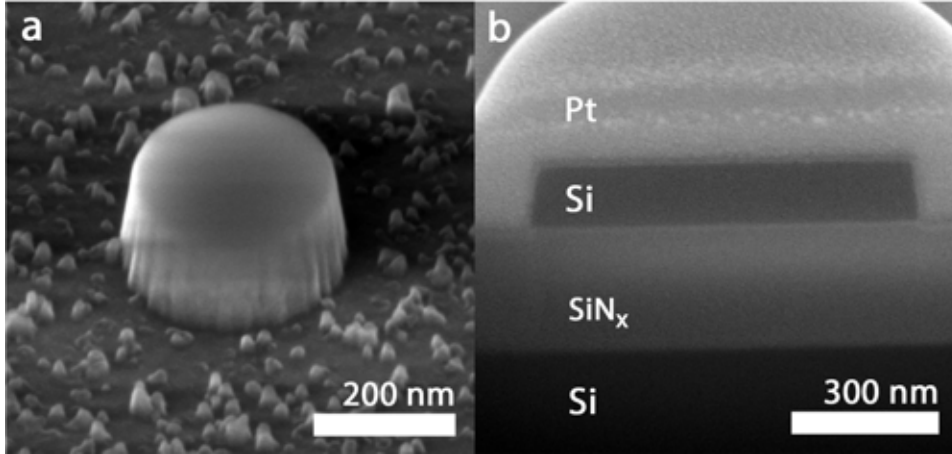


Figure 4.3: (a) High resolution secondary electron image of a 260 nm Si resonator on silicon nitride under a tilt of 45°. The small particles on the substrate are non-removable residues from the fabrication process and are not supposed to interfere with the CL measurement. (b) Focused ion beam cross section through a 600 nm resonator. The bright top layer is the protective platinum, deposited prior to the cross section. The resonator rests on the visible Si₃N₄ layer.

4.2 Cathodoluminescence Measurements

In the following, the measurement results are discussed, beginning with an investigation of the background signal's time dependence and continuing with the spatially and spectrally resolved polarimetry measurements before coming to angular examination of the far-field.

4.2.1 Evaluation of Background Signal

Before performing polarimetry measurements on the newly fabricated sample, it is important to evaluate the level and the stability of the background radiation. The spectral shape of the silicon nitride reference is plotted in [Figure 4.4a](#). It is determined by one main feature at 580 nm and two side peaks at 450 nm and 750 nm. The silicon layer on top reduces the emission of the 580 nm peak and adds another peak around 685 nm. Except for the top of this peak, the silicon reference is below the nitride reference, suggesting that the background signal is mainly emitted from within the Si₃N₄ layer and significantly reduced by absorption in the covering silicon layer. The peak at 685 nm is attributed to a second order Fabry P  rot mode in the Si₃N₄ layer, since the refractive index of ~ 2.18 of the LPCVD Si₃N₄ leads to 312 nm wavelength in the nitride, which is close to the measured layer thickness. The 7 nm difference to the measured thickness of 319 nm can be explained by a change of the layer composition during the annealing process, influencing the optical constants.

Besides the standard reference measurements on a silicon pad and the bare nitride

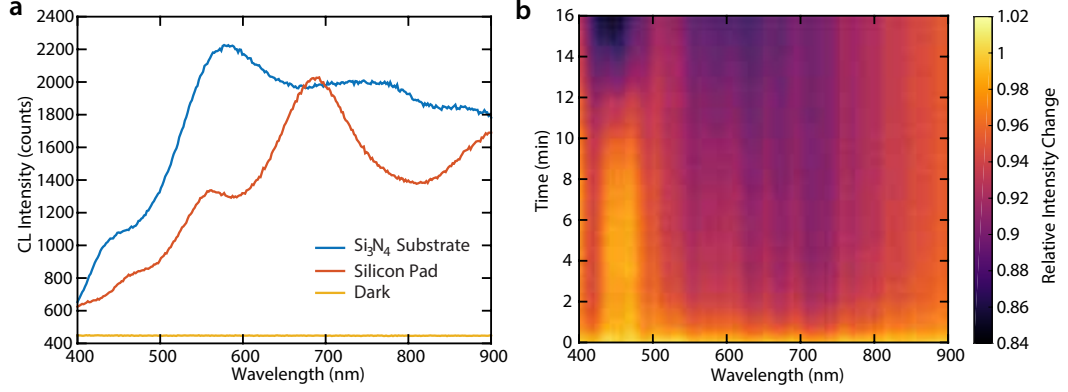


Figure 4.4: (a) background signal measured on the silicon nitride substrate as well as on a large silicon pad on the nitride layer, together with the dark reference. The system response is not taken into account. (b) Time dependent relative change of the background intensity measured on a single spot on the silicon nitride layer. The initial spectrum was calculated as the mean of the first four spectra which is an average over 1.6 s. The data was acquired using a beam voltage of 30 keV and a current between 9 nA and 10 nA.

layer, a CL spectrum is recorded every 0.4 s while the electron beam is focused at a single spot on the silicon nitride substrate. A 2D-plot (Figure 4.4b) of the spectra then provides the time dependence of the background radiation. The presented spectra in Figure 4.4 are normalized to the initial intensity $I(\omega)$ measured at the beginning of the measurement. The emission at wavelengths above 500 nm seems quite stable after a small intensity loss of about 5% during the first minute. The feature between 400 nm and 500 nm is more stable for the first 10 min of irradiation, but then loses about 15% of its intensity. Both results promise advantages over the SiO₂ based sample design. Firstly, even with 10 times higher current compared to the measurements in Section 3.3, the total measured intensity is three times smaller than the highest background intensities of the old sample design. Secondly, the change of intensity with time is much less severe and a pre-irradiation of about 15 min promises to be sufficient to stabilize the emission.

4.2.2 Polarimetry Measurements

Polarimetry measurements using the same beam settings were performed on multiple resonators of which the two examples of 200 nm and 260 nm diameter are discussed in the following. This selection is motivated by the need for a limited number of modes being separately addressable as an upper size limit. The lower size limit is determined by the desired spatial resolution in both spectral and angular measurements, which is affected by the electric field extent of the beam and beam drift due to charging of

the sample.

Spatially Resolved Spectral Polarimetry

Spectral polarimetry is performed to obtain an impression of the existing modes in the resonator. As most important measures the DOLP and DOCP for both investigated resonators are presented in [Figure 4.5](#). For spatial analysis, the cylindrical resonators are divided into circles with a specific central radius and fixed width. Subsequently, the CL spectra from the pixel within each circle are averaged for each of the six polarimetry measurements (see inset in [Figure 4.5c](#)). Thus, it is possible to correlate the data for a certain radius in all six measurements. The results are plotted as 2D images with wavelengths on the vertical axis and radius on the horizontal axis.

Comparing the results for both resonators reveals similarities above 650 nm and below 450 nm where the DOLP has clearly distinguishable features which are strongest in the center of the resonator. The 200 nm particle shows another feature between 54 nm and 90 nm radius emitting around 500 nm. At the same spatial region a small DOLP is visible for shorter wavelengths. As the particle size increases to 260 nm the feature at 500 nm emission wavelength shifts spectrally and spatially, represented by the feature around 100 nm radius at $\lambda = 600$ nm in image [Figure 4.5b](#), which matches the relative position within the particle. Furthermore, additional features show up or are at least more clearly separated by dark regions of small DOLP. These are located at 450 nm and 525 nm close to the particle edge and around 550 nm in its center. For the DOCP in [Figure 4.5c,d](#) a value close to zero is expected due to the nature of the electric and magnetic dipole and quadrupole modes. The measured DOCP takes absolute values below 0.05 for most regions in the plot, which is a reasonable value since the background signal is not perfectly stable. Below 450 nm the DOCP shows a significant right handedness, however these wavelengths are at the edge of the working bandwidth of the QWP and additionally the absolute detected intensity (see [Section A.3.1](#)) is close to the dark reference and thus more sensitive to small variations. The discussed characteristics of the emission are confirmed regarding the linearly polarized intensity, which takes into account the spectral shape of the total intensity and is plotted in [Figure A.4](#).

The spatially and wavelength resolved polarimetry measurements show that different definite features distribute to the DOLP at wavelength dependent on resonator size and excitation position. For the following angular analysis three candidates matching available bandpass filters are identified from the spectral data. Firstly, the feature around 500 nm at the edge of the 200 nm particle and secondly and thirdly the wavelengths 550 nm and 600 nm for measurements at the edge and center of the larger particle.

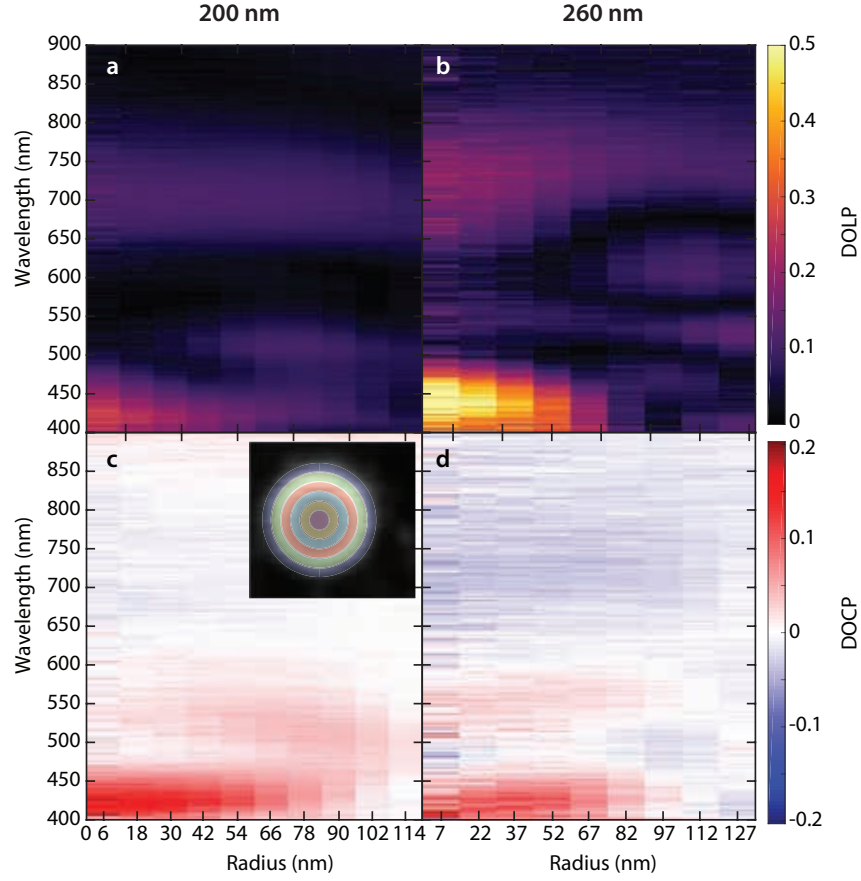


Figure 4.5: The spectrally resolved DOLP (a,b) and DOCP (b,c) for the 200 nm diameter (left) and the 260 nm resonator (right). The rotational symmetry of the particle motivates averaging of the 2d CL map along circles with different radius to demonstrate the spatial dependence of measured resonances. The areas for these averages are sketched as colored regions on the 200 nm particle in the inset of (c). (a) and (b) show consistent features at the limits of sensitivity below 400 nm and above 700 nm. Different features are visible close to the particle edges at larger radii for both particle sizes. On the larger particle multiple resonances become visible, distributed over the whole particle. The DOCP in (c) and (d) is close to zero except for a region below 450 nm which is at the edge of the regime where the QWP works reliably. The corresponding total and linearly polarized intensities are shown in [Figure A.4](#)

Angular Polarimetry

For the angular polarimetry measurements a current of 10 nA has been chosen allowing for an integration time of 60 s. Again, a change of the particle under study was necessary after three to four full polarimetry measurements at different wavelengths to prevent effects from sample degradation as discussed in [Section A.4](#). Before any measurements, each region was irradiated once for 15 min to 20 min with the same beam current. The results of the polarimetry measurements are compared in [Figure 4.6](#). The DOCP is not shown because of its small absolute values and the absence of directional features (see [Section A.3.2](#)). In all measured DOLP datasets, higher values at angles θ close to 90° are observable as for the previous sample design ([Figure 3.9](#)). For their interpretation the same considerations as in [Section 3.3.2](#) need to be taken into account. Due to the Lambertian emission pattern of the incoherent background radiation, the collected intensities at grazing angles are small, leading to higher uncertainties and a larger polarized component. The polarizing effect of the substrate/air interface discussed in [Section A.1](#) is small and centered at different wavelengths, hence it is neglected for the interpretation. The emission at central excitation of the 260 nm diameter particle is characterized by a S_0 emitting mainly in vertical direction whereas the $DOLP$ is highest at grazing angles. Thus, the small $DOLP$ in the center have an effect on the polarized intensity $DOLP \times S_0$ which is shown in [Figure A.6](#). This indicates some similarities to a combination of modes measured previously ^[16].

While exciting the center of the particle, the emission pattern is highly symmetric towards large θ with less polarized upwards emission for both particles at most wavelengths. Moving the electron beam to the right edge of a particle induces a higher DOLP for upwards oriented radiation while the polarization at large θ undergoes only small changes. Due to the non symmetric excitation, directional beaming can be observed for the presented wavelengths, which does not appear for every detection wavelength. It manifests as a higher DOLP at one or the other side of the central hole in the bottom plots of [Figure 4.6](#). Interestingly, radiation is steered in the forward direction at 500 nm and 550 nm for the small, respectively the large resonator, but backwards at 600 nm (large resonator). A corresponding flip in directionality could not be observed on the 200 nm particle. Directional scattering in dielectric and plasmonic nano particles is well known and commonly referred to as Kerker scattering^[21–24]. It is based on the interference of overlapping modes. An example of a magnetic and electric dipole is sketched in [Figure 4.7](#). In case the modes spectrally overlap each other, the resonances will either be in phase or out of phase, depending on the spectral positions of the resonance. This phase relation can lead to constructive interference towards one direction and destructive interference towards the other as sketched in [Figure 4.7](#) by the parallel and anti-parallel green arrows of the electric fields in the MD and ED mode. For wavelengths away from the resonance, the polarized emission has the same directivity as the total emitted intensity. In [Figure 4.6](#), this shows up as flip in the direction of emission for linearly polarized light.

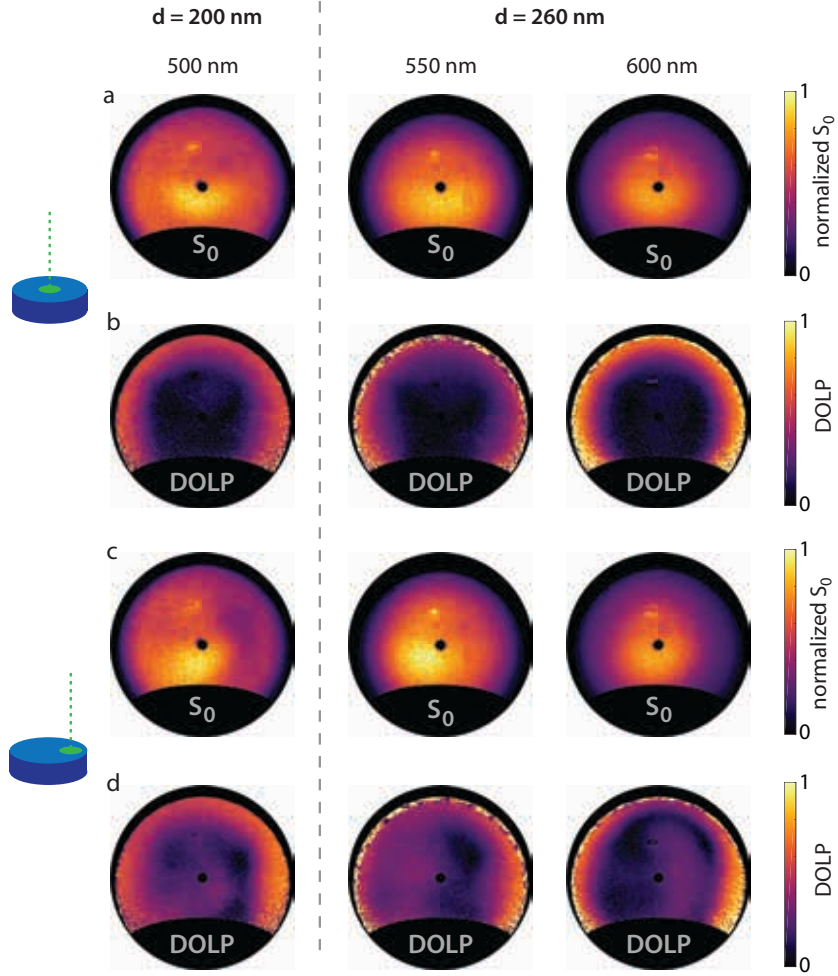


Figure 4.6: Angular emission profile of linearly polarized light components for both particles at 500 nm for the 200 nm diameter resonator and 550 nm and 600 nm for the 600 nm diameter resonator. The two top rows plot the emission as the particle is excited in the center whereas for the images in the two bottom rows the resonators have been excited close to their right edge. All DOLP plots show strong linear polarization at large angles θ whereas only the off center excited particles exhibit polarized emission with upward components. The total intensity is dominated by Lambertian like emission upwards at small angles θ .

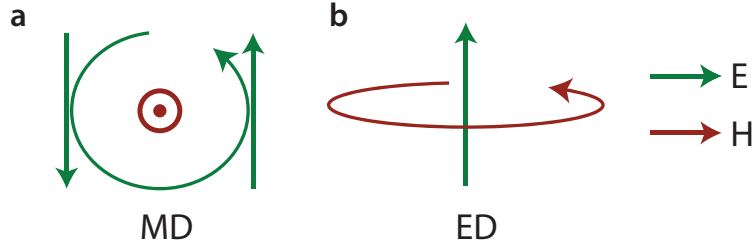


Figure 4.7: The fields of a magnetic and electric dipole mode in vicinity of the emitting particle are sketched. If both are in phase, the fields can only interfere constructively towards one direction.

Additional information about the orientation of the linearly polarized light can be obtained from the electric field components. For each point in the angular dataset, the horizontal and vertical field is calculated according to equations (2.10) to (2.12) and subsequently translated to the spherical components E_θ and E_ϕ which are parallel to the corresponding unit vectors of the θ and ϕ directions and perpendicular to the propagation direction. Figure 4.8 presents the detected field amplitudes of polarized light at 550 nm and 600 nm emission wavelength for both excitation positions. In case

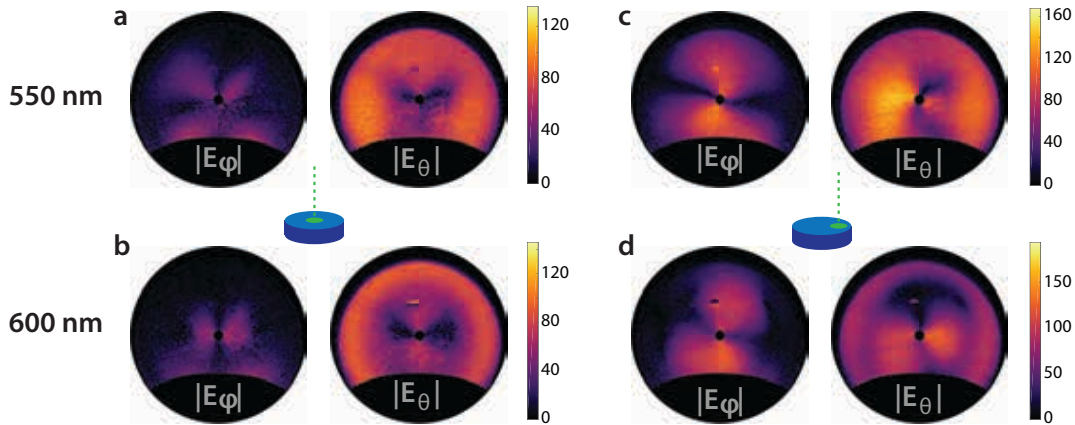


Figure 4.8: The obtained field amplitudes for 550 nm (a,c) and 600 nm (b,d) emission from the 260 nm resonator for both excitation positions at center (a,b) and edge (c,d) of the resonator. The components ϕ and θ of the electric field are perpendicular to each other and the direction of the emitted radiation.

of central excitation, the smaller amplitude of E_ϕ attracts attention. The two plots of $|E_\phi|$ at the left of Figure 4.8 exhibit a fourfold symmetry, which can be attributed to the imperfect correction routine for the mirror's effect on the polarization. Similar behavior has been observed before^[20]. The downward shift which can be observed from 550 nm to 600 nm suggests a difference in $|E_\phi|$ between the measurements but

due to the artificial perturbation from the mirror this difference cannot be analyzed thoroughly. Most of the polarized emission is parallel to the θ direction. At central excitation, the θ field component at 600 nm is slightly more confined into a ring at large θ than at 550 nm. In vicinity of the center, two dark spots at the left and right side of the hole as well as two bright features above and below the hole are visible. Changing to antisymmetric excitation close to the particle edge leads to higher amplitudes of the polarized fields. In $|E_\phi|$, the effect of the mirror imperfectness vanishes under the larger measured amplitudes, which for both wavelengths show a symmetric pattern above and below a vertical symmetry line through the image centers. This symmetry corresponds to the vertical move from central to edge excitation. The observed increase in polarization originates from the higher probability to couple to in plane modes, oscillating perpendicular to the z direction. Again, $|E_\theta|$ exhibits a feature with two regions of lower intensity and two of higher intensity, this time relatively rotated by 90° compared to the result for central excitation. At 550 nm, the θ component has a stronger amplitude towards the left as could be expected from the previous results whereas at 600 nm, the amplitude of the fields in both directions is more symmetric. The ring in $|E_\theta|$ at 600 nm, appearing at large angles θ is thinner under antisymmetric excitation than in case of central excitation.

The angular polarimetry measurements show consistent behavior at large θ compared to the previous sample design. Additionally, the flip in directionality of the emission of linearly polarized light between 550 nm and 600 nm on the larger resonator (Figure 4.6) as well as the wavelength and excitation position dependent field amplitudes (Figure 4.8) indicate the detection of dielectric modes. As a next step, the calculated fields are compared to simulated far-field emission patterns of different dielectric modes in the disc Mie resonators.

4.3 Eigenmode Simulations

Finite-element frequency-domain eigenfrequency studies were performed in COMSOL Multiphysics, providing the electromagnetic field of an isolated eigenmode of the geometry at any point in the simulated space. The far-field is subsequently calculated from the known field on a closed interface around the resonator particle. The eigenfrequencies are determined by searching in a given frequency band for those frequencies which overcome a fixed loss limit. Due to time constraints, the simulation parameters were optimized for performance more than for accuracy. Thus, parasitic results such as resonances which are only supported by boundary layers or sharp edges in the geometry can appear in the output and need to be filtered manually by discarding all modes which have high losses or an unphysical field distribution within the sample. For the selected real eigenmodes the far-field projection is calculated and translated into a θ and ϕ dependent dataset. Due to the rotation symmetry of the Mie resonators, the calculated far-field pattern needs to be averaged azimuthally to be comparable to the experimental CL results.

First, the simulated absolute electric field amplitude in the far-field is investigated. Since the radiation from the simulated eigenmodes of the resonator is linearly polarized, the electric field amplitude corresponds to the measured linearly polarized intensity, given by $DOLP \times S_0$ (see Figure 4.6 and Figure A.6). Figure 4.9 displays the field amplitudes for eight resonances located around 570 nm (row a) and 490 nm (row b). The exact spectral location of the modes depends on the simulation's geometry and settings and is thus only a qualitative entity. The far-field radiation pattern is obtained by a projection of the simulated fields on a defined closed surface around the resonator onto a sphere with 1 m radius. Thus, all calculated fields in the simulation are consistent. However, since in the experiment the electron beam excites each mode in a unique way, the simulated intensities do not directly indicate the probability with which a certain mode is detected and hence the relative intensities of different modes cannot be related to measured intensities. All plots in Figure 4.9 show a high

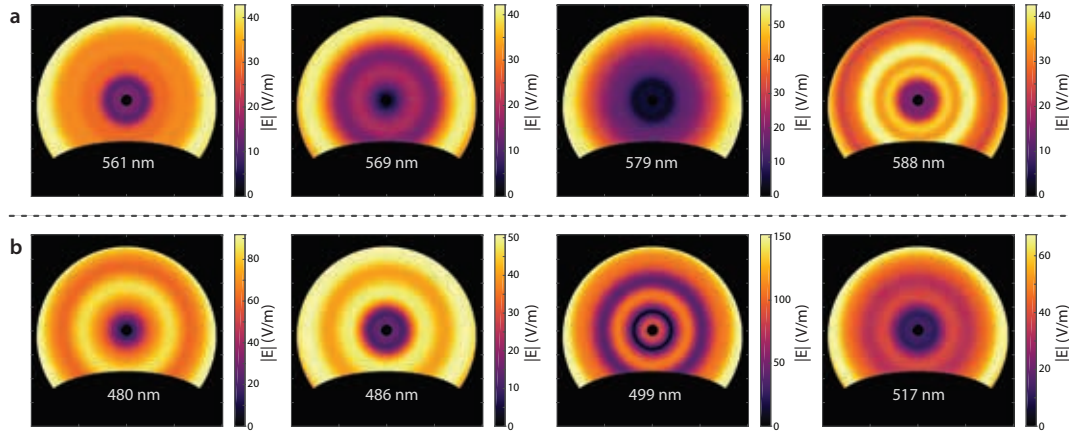


Figure 4.9: Amplitude of the total electric field for four calculated resonances around 570 nm (a) and 490 nm (b). The amplitudes are comparable since all were obtained using the same calculation routine.

intensity towards grazing angles, matching the measurement outcome in Figure 4.6 and Figure 3.9 where the DOLP is high at large θ . Since the calculated modes are spectrally close to each other and can propagate through the same 40 nm bandwidth bandpass-filter, it is likely that a superposition of them is measured in the experiment, which leads to high intensity at grazing angles and an overlap of features in the central region.

Next, by comparing the calculated fields E_ϕ and E_θ separately, all available information is used to compare simulation and experiment. Most of the calculated E_ϕ far-field patterns are dominated by bright features at large θ which are not present in the experimental results in Figure 4.8. From the measured results in Figure 4.8, an E_ϕ which is dominated by upward emission and an E_θ with high intensity at larger θ are expected. Additionally, the modes are expected to have a significant z-component of the electrical field in the resonator, which promotes efficient excitation

with the electron beam. For two calculated modes which show similar behavior to this, and match the measured wavelengths of (550 ± 20) nm and (600 ± 20) nm, the field amplitudes for E_θ and E_ϕ are plotted in Figure 4.10a,b. For the 552 nm resonance, E_ϕ shows highest intensity at small θ and small intensity at larger angles corresponding to the trend observed in Figure 4.8c. Also the fact that E_θ is strongest at non grazing angles in the simulation appears in the experiment. At 600 nm the large amplitude of E_θ at grazing angles in the calculation can be found as the high intensity ring in the experiment (Figure 4.8b,d). However, the ring patterns and low intensities at small θ in all simulated far-fields are not well represented in the experimental result. Therefore it is not possible to prove that the simulated modes correspond to the measured emission patterns.

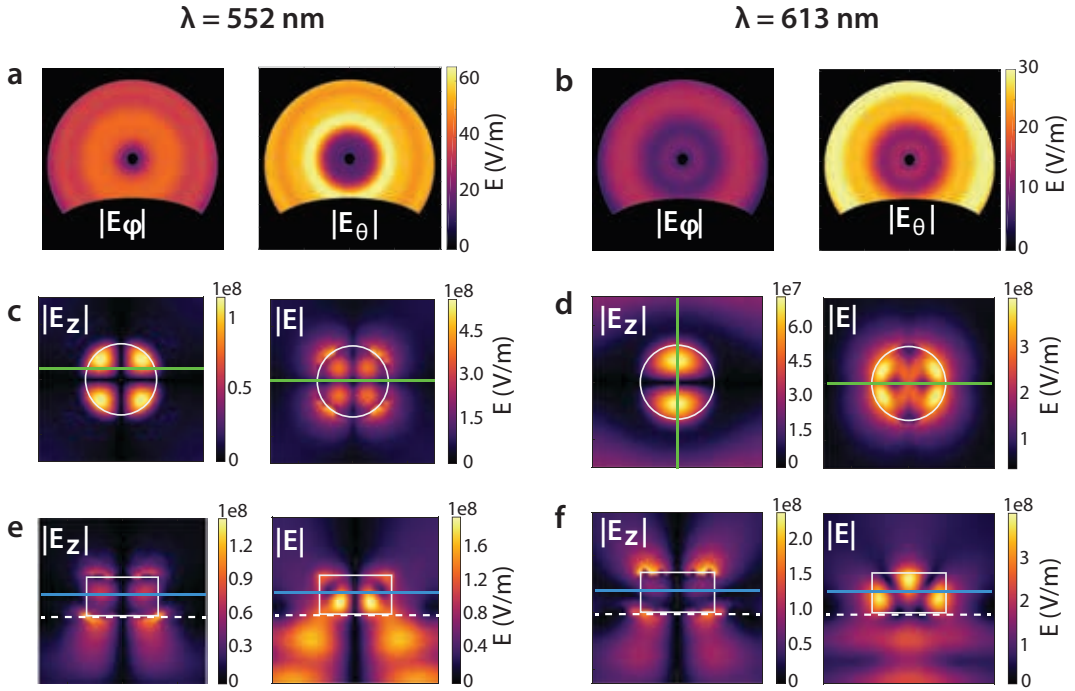


Figure 4.10: (a),(b) The calculated far-field amplitudes of E_ϕ and E_θ for eigenmodes at 552 nm and 613 nm calculated for a resonator with 260 nm diameter. (c-f) The field distribution of $|E_z|$ and $|E|$ in the resonator and its vicinity. The green/blue lines correspond to the location of the cross sections beneath/above the plot. The white circle (c,d) and rectangle (e,f) indicate the resonator on the substrate (white dashed line).

A horizontal cross section of the field profile of $|E_z|$ and $|E|$ within the particle and its surroundings is plotted in Figure 4.10c,d and a vertical cross section is displayed in e and f in the same figure. The green and blue lines in the cross sections indicate the positions of the other respective cross section. Comparing the amplitude of $|E_z|$ with the total field amplitude $|E|$ shows that the mode is dominated by a field in z-direction in certain regions in the particle. Thus, excitation with the electron beam is feasible.

The field profiles of both modes exhibit a higher amplitude of $|E_z|$ at regions closer to the edge of the resonator (Figure 4.10c,e), which indicates an increased probability to excite the particle. This matches the appearing linearly polarized features at smaller θ when the electron beam is incident close to the right edge of the particle in Figure 4.6c,d. However, this result can also be explained by more efficient outcoupling of light if the particle is excited at its edge.

Combining theoretical and experimental results provides valuable details, helping to understand the system better even though the calculated modes could not be matched to the experimental result with a high degree of certainty. Firstly, the presence of a strongly linearly polarized part at grazing angles in measurement and simulation shows that the modes in the investigated dielectric resonators tend to emit a significant part of their energy in the radial direction when excited by electron beam irradiation. The directionality towards those angles (Figure A.6) is even more pronounced than in transition radiation on metals^[25].

Secondly, it is possible to use the experimentally determined field amplitudes to restrict the number of theoretically calculated modes, which can be responsible for the measured emission patterns. This approach is insensitive to uncertainties in the calculated eigenfrequencies and thus to small mismatches between simulation and experimental geometry since the wavelength of the modes does only depend on the dimensions of the resonator.

Thirdly, a study of the field distribution in the particles also helps discard some of the simulated modes since successful excitation is more probable if the z-component of the electric field is large at the excitation position. Fourthly, there is available information about the different modes in the directionality of emission. This information has not been fully exploited since the calculated modes are eigenmodes of the geometry, but are affected by the excitation manner and position in the experiment, for instance because the most efficient excitation positions are off-center, which breaks the symmetry of the particle and of the emission (see measurements in Figures 4.6, 4.8 and A.6). In order to investigate the influence of excitation position on the far-field radiation pattern, the knowledge of the calculated eigenmodes could be used to modify the driving source in FDTD simulations to only couple to a specific mode. The far-field emission pattern from the FDTD simulation could then be compared to the measurement.

The experimental and theoretical investigation of silicon resonators on silicon nitride substrates has provided detailed information about the spectral and spatial position of resonances in the particles. The linearly polarized part, the polarized intensity and the orthogonal fields of the angular emission have been compared to simulated results and consistent behavior has been identified. In order to draw reliable connections from the measured emission pattern to individual calculated modes, the spectral resolution of the angular measurement needs to be increased or the overlap between different modes needs to be reduced by geometry adjustment.

5 Conclusions

Nanostructures for optics and photonics create a great wealth of possibilities for research and engineering in the field of light. This thesis combines two key elements of research in nanophotonics. Firstly, fundamental research on dielectric nanostructures is required to understand the different ongoing processes. In particular Mie resonators are of interest due to their low intrinsic losses in the regime of visible light and their tunable electric and magnetic resonances, which enable novel optical applications such as metasurfaces [1,3–5,23]. The investigation of these structures at the nanoscale plays a key issue in nanophotonics. Secondly, new experimental methods need to be developed in order to investigate samples which interact with light at the nanoscale. One of these techniques, cathodoluminescence imaging spectroscopy has yielded outstanding results in recent years [12,13,26,27]. This technique benefits from the high spatial resolution of electron microscopy and from the versatility of optical measurements. By introducing optical polarimetry to cathodoluminescence measurements, the full polarization state of light can be determined. Together with measuring the wavelength and propagation direction, all major degrees of freedom of the emitted light from a nanostructure can be characterized [20]. In this research it enabled the detection of light emitted by dielectric modes even though these are covered by a large incoherent background, originating from electron-hole pair recombination luminescence in the substrate.

For performing this research, high quality silicon Mie resonators on a silicon oxide layer were fabricated by electron-beam lithography and reactive-ion-etching. The electron-beam induced radiation from the resonators has been measured in a wavelength-, polarization- and angle-resolved way with ~ 20 nm resolution of the excitation position. Spatially and spectrally resolved CL maps provided information about the mode profile in the resonator after application of a background correction routine which takes a time dependent change of the background into account. This time dependent variation of background intensity could be attributed to electron-beam induced defect excitation and creation in the underlying silicon oxide layer. It was identified as a major source of error in polarimetry measurements, which depend on the identical total intensity for the measurements of six polarization configurations. A preceding 30 min electron beam irradiation was applied to create an equilibrium of the defect excitation such that the polarimetry measurements were conducted with a stable background signal.

The measurements discussed in [Section 3.3.2](#) and [Section 3.3.2](#) could discriminate the linearly polarized coherent signal from the dielectric resonators from the unpolarized incoherent background signal. The fact that distinct circularly polarized features

have not been observed matches the expectation for the emission from electric and magnetic dipole and quadrupole modes. The comparison of the retrieved signal with finite-difference time-domain simulations (Section 3.2) shows good agreement in the position of the excited resonances and their red-shift as particle size increases. Angle-resolved polarimetry measurements show some linearly polarized features in the measured far-field, but due to the large background radiation their contrast was too low to identify distinct patterns which could have been used to draw a connection to simulated emission patterns. For this reason, an improved sample design based on silicon nitride substrate, known to have less defects and thus less CL background signal is introduced.

Spatially resolved polarimetry measurements on the new set of silicon resonators exhibit clearly visible linearly polarized features, which depend on excitation position and shift spectrally as particle size increases. Angular polarimetry measurements were performed to further investigate these features. In the case of asymmetric excitation, an inversion of emission direction for different wavelengths was observed as an effect of the interference of two overlapping dielectric modes of the resonator. The discussed angle resolved polarimetry measurements exhibit a linearly polarized feature at high angles θ . In order to use the full information provided by polarimetry, the perpendicular fields E_θ and E_ϕ are determined. Most intensity of the emitted radiation is carried by E_θ whereas the amplitude of E_ϕ becomes significant when the particle is excited at the edge, as could be expected from breaking the symmetry.

Finite-element frequency-domain eigenmode simulations were performed to obtain the field distribution in the particle and the far-field emission pattern of the individual eigenmodes. A comparison of the total amplitude in the calculated far-field with the experiment shows that the bright intensity at grazing angles is characteristic for the emission of several dielectric resonances. The wavelength differences between most of the calculated eigenmodes is smaller than the bandwidth of the bandpass filter used in angular measurements and hence it is likely that a superposition of the radiation of different modes is measured in the experiment. This is in agreement with the presence of broad features without a distinctive shape in the angle range up to $\theta = 70^\circ$ in the experimental results (Figure 4.6 and Figure A.6). Due to the difference between the eigenmode calculations, which do not require a source, and the experiment where the electron beam is a spatially confined source, it is not possible to compare the calculated far-field patterns one-to-one to the measured fields, especially in the case of asymmetrical excitation. However, the main features of the excited modes can be found in both simulation and experiment. Combining the far-field calculations from finite-element eigenmode simulations with those from finite-differential time-domain simulations can provide the necessary information, since the latter requires a source, adjustable to individually drive the calculated eigenmodes.

In summary, this research has validated the approach of using polarimetry to discriminate between incoherent background radiation and coherent emission from dielectric modes when the signal is dominated by the background. Possible ways to correct for a changing background due to defect creation were applied and discussed,

which is a valuable contribution to the arsenal of CL measurements. The capability of cathodoluminescence polarimetry to fully characterize dielectric eigenmodes in nanoscale resonators has been evaluated. Although definitive one-to-one attributions of measurements to specific modes were not possible, the selection could be narrowed down to a few modes. In addition, several lessons and guidelines were distilled to aid in future research. Firstly, the background of the samples needs to be stable within a timescale of several minutes depending on the integration time. Secondly, the degrees of polarization can be used as an indicator for the presence of modes, however in order to compare measurements and simulations quantitatively, the intensity of the polarized light ($DOLP \times S_0$; $DOP \times S_0$) needs to be regarded. Thirdly, the investigated resonances should have only little spatial and spectral overlap to ensure separate excitation and detection respectively. This can be achieved by a careful sample design. Lastly, eigenmode calculations in COMSOL Multiphysics can be used to determine the characteristics of the resonances. The calculated resonances can then be addressed in FDTD simulations which are capable of reproducing the dependence of excitation location.

Despite the fact that perfect modal recognition could not be achieved, the knowledge about the modes and the capabilities of cathodoluminescence polarimetry to measure them has been improved. Thanks to this thesis, there is a clear way forward for future research on the topic.

Bibliography

- [1] S. Jahani and Z. Jacob. All-dielectric metamaterials. *Nature Nanotechnology*, 11(1):23–36, 2016. ISSN 1748-3387. doi: 10.1038/nnano.2015.304. URL <http://www.nature.com/doifinder/10.1038/nnano.2015.304>.
- [2] A.F. Koenderink, A. Alu, and A. Polman. Nanophotonics: Shrinking light-based technology. *Science*, 348(6234):516–521, 2015. ISSN 0036-8075. doi: 10.1126/science.1261243.
- [3] P. Spinelli, M. Verschuuren, and A. Polman. Broadband omnidirectional antireflection coating based on subwavelength surface Mie resonators. *Nature communications*, 3:692, 2012.
- [4] M. L. Brongersma, Y. Cui, and S. Fan. Light management for photovoltaics using high-index nanostructures. *Nature materials*, 13(5):451–60, 2014. ISSN 1476-1122. doi: 10.1038/nmat3921. URL <http://www.ncbi.nlm.nih.gov/pubmed/24751773>.
- [5] J. v. d. Groep and A. Polman. Designing dielectric resonators on substrates : Combining magnetic and electric resonances. *Optics Express*, 21(22):1253–1257, 2013. ISSN 1094-4087. doi: 10.1364/OE.21.026285.
- [6] E. Abbe. VII.-On the Estimation of Aperture in the Microscope. *Journal of the Royal Microscopical Society*, 1(3):388–423, 1881.
- [7] T. G. Habteyes, I. Staude, K. E. Chong, J. Dominguez, M. Decker, A. Miroshnichenko, Y. Kivshar, and I. Brener. Near-Field Mapping of Optical Modes on All-Dielectric Silicon Nanodisks. *ACS Photonics*, 1(9):794–798, 2014. ISSN 23304022. doi: 10.1021/ph500232u.
- [8] L. De Broglie. Waves and Quanta. *Nature*, 112:540, 1923.
- [9] F. J. García De Abajo. Optical excitations in electron microscopy. *Reviews of Modern Physics*, 82(1):209–275, 2010. ISSN 00346861. doi: 10.1103/RevModPhys.82.209.
- [10] M. Kuttge. *Cathodoluminescence plasmon microscopy*. 2009. ISBN 978-90-77209-32-5. URL <http://www-old.amolf.nl/publications/theses/kuttge/kuttge.html>.
- [11] E. J. R. Vesseur. *Electron Beam Imaging and Spectroscopy of Plasmonic Nanoantenna Resonances*. 2011. ISBN 9789077209516.

- [12] T. Coenen. *Angle-resolved cathodoluminescence nanoscopy*. Amsterdam, 2014. ISBN 9789462591622.
- [13] B. J. M. Brenny. *Probing Light Emission At the Nanoscale With Cathodoluminescence*. 2016. ISBN 9789492323040.
- [14] T. Coenen and A. Polman. Polarization-sensitive cathodoluminescence Fourier microscopy. *Optics Express*, 20(17):18679, 2012. ISSN 1094-4087. doi: 10.1364/OE.20.018679.
- [15] P. Das, T. K. Chini, and J. Pond. Probing higher order surface plasmon modes on individual truncated tetrahedral gold nanoparticle using cathodoluminescence imaging and spectroscopy combined with FDTD simulations. *Journal of Physical Chemistry C*, 116(29):15610–15619, 2012. ISSN 19327447. doi: 10.1021/jp3047533.
- [16] T. Coenen, J. Van De Groep, and A. Polman. Resonant modes of single silicon nanocavities excited by electron irradiation. *ACS Nano*, 7(2):1689–1698, 2013. ISSN 19360851. doi: 10.1021/nm3056862.
- [17] M. a. S. Kalceff and M. R. Phillips. Cathodoluminescence microcharacterization of the defect structure of quartz. *Physical Review B*, 52(5):3122–3134, 1995. ISSN 01631829. doi: 10.1103/PhysRevB.52.3122.
- [18] H.-J. Fitting, A. N. Trukhin, T. Barfels, B. Schmidt, and A. v. Czarnowski. Radiation induced defects in SiO₂. *Radiation Effects and Defects in Solids*, 157(6-12):575–581, jan 2002. ISSN 1042-0150. doi: 10.1080/10420150215756. URL <http://www.tandfonline.com/doi/abs/10.1080/10420150215756>.
- [19] E. P. O'Reilly and J. Robertson. Theory of defects in vitreous silicon dioxide. *Physical Review B*, 27(6):3780–3795, 1983. ISSN 01631829. doi: 10.1103/PhysRevB.27.3780.
- [20] C. I. Osorio, T. Coenen, B. J. M. Brenny, A. Polman, and A. F. Koenderink. Angle-Resolved Cathodoluminescence Imaging Polarimetry. *ACS Photonics*, 3(1):147–154, 2016. ISSN 23304022. doi: 10.1021/acsp Photonics.5b00596.
- [21] M. Kerker, D.-S. Wang, and C. L. Giles. Electromagnetic scattering by magnetic spheres. *Journal of the Optical Society of America*, 73(6):765, 1983. ISSN 0030-3941. doi: 10.1364/JOSA.73.000765. URL <http://dx.doi.org/10.1364/JOSA.73.000765>.
- [22] B. Rolly, B. Stout, and N. Bonod. Boosting the directivity of optical antennas with magnetic and electric dipolar resonant particles. *Optics Express*, 20(18):20376, 2012. ISSN 1094-4087. doi: 10.1364/OE.20.020376.
- [23] I. Staude, A. E. Miroshnichenko, M. Decker, N. T. Fofang, S. Liu, E. Gonzales, J. Dominguez, T. S. Luk, D. N. Neshev, I. Brener, and Y. Kivshar. Tailoring directional scattering through magnetic and electric resonances in subwavelength

- silicon nanodisks. *ACS Nano*, 7(9):7824–7832, 2013. ISSN 19360851. doi: 10.1021/nn402736f.
- [24] T. Coenen, F. Bernal Arango, A. Femius Koenderink, and A. Polman. Directional emission from a single plasmonic scatterer. *Nature communications*, 5:3250, 2014. ISSN 2041-1723. doi: 10.1038/ncomms4250. URL <http://www.ncbi.nlm.nih.gov/pubmed/24488237>.
- [25] B. J. M. Brenny, T. Coenen, and A. Polman. Quantifying coherent and incoherent cathodoluminescence in semiconductors and metals. *Journal of Applied Physics*, 115(24), 2014. ISSN 10897550. doi: 10.1063/1.4885426.
- [26] T. Coenen, E. J. R. Vesseur, and A. Polman. Angle-resolved cathodoluminescence spectroscopy. *Applied Physics Letters*, 99(14):4–6, 2011. ISSN 00036951. doi: 10.1063/1.3644985.
- [27] T. Coenen, B. J. Brenny, E. J. Vesseur, and A. Polman. Cathodoluminescence microscopy: Optical imaging and spectroscopy with deep-subwavelength resolution. *MRS Bulletin*, 40(04):359–365, 2015. ISSN 0883-7694. doi: 10.1557/mrs.2015.64. URL http://www.journals.cambridge.org/abstract/_S0883769415000640.
- [28] E. Hecht and A. Zajac. *Optics 4th (International) Edition*. Addison Wesley publishing company, 4 edition, 2002. ISBN 0321188780.
- [29] E. F. Schubert, T. Gessmann, and J. K. Kim. *Light emitting diodes*. Wiley Online Library, 2005.

A Appendix

A.1 Polarization of Background Luminescence from the Substrate Interface

Although the radiation from electron-hole pair recombination at defect centers and inter-band transitions in the silicon oxide substrate is random in phase and polarization, the polarization dependent transmission and reflection coefficients of the substrate/air can polarize the transmitted light. The transmission for s- and p-polarized light is given by [28]

$$T_s = 1 - \left(\frac{n_1 \cos \theta_{in} - n_2 \sqrt{1 - \sin^2 \theta_t}}{n_1 \cos \theta_{in} + n_2 \sqrt{1 - \sin^2 \theta_t}} \right)^2 \quad (\text{A.1})$$

$$T_p = 1 - \left(\frac{n_2 \sqrt{1 - \sin^2 \theta_t} - n_1 \cos \theta_{in}}{n_2 \sqrt{1 - \sin^2 \theta_t} + n_1 \cos \theta_{in}} \right)^2 \quad (\text{A.2})$$

$$\text{with } \theta_{in} = \sin^{-1} \left(\frac{n_2}{n_1} \sin \theta_t \right). \quad (\text{A.3})$$

The inset of [Figure A.1a](#) sketches the geometry.

The plots in [Figure A.1a,d](#) show the transmission for both polarizations through a SiO_2 ($n_1 = 1.458$)/air ($n_2 = 1$) (plot a) and a Si_3N_4 ($n_1 = 2.15$ and 2.25)/air (plot d) interface. The refractive index n for silicon oxide is assumed constant for the visible range, the n of silicon nitride was determined by optical ellipsometry as discussed in [Section 4.1](#), [Figure 4.1](#). Since the recombination centers are located within the substrate, the angular dependence of the emitted intensity is of Lambertian shape ($I_0 \propto \cos \theta_t$) [29] as follows from Snell's law of diffraction. Consequently, the emitted normalized intensity of s- and p-polarized light becomes $I_{s,p}(\theta_t) = T_{s,p}(\theta_t) \cos \theta_t$. [Figure A.1](#) shows the angle dependent transmitted intensity for the SiO_2 based (plots b,c) and the Si_3N_4 based (plots e,f) sample geometry as normal plots and in polar representation. The polarized part of the emission is determined by the difference $I_{p-s} = I_p - I_s$, which is plotted as purple curves in [Figure A.1](#).

The polarizing effect of the different transmission of s- and p-polarized light is strongest between angles between 50° and 75° , and peaks to $\sim 10\%$ for the SiO_2 geometry and $\sim 20\%$ for the Si_3N_4 geometry. Thus its contribution is negligible for nearly all angles for the silicon oxide based sample but significant for angles larger than 60° for the nitride based sample. However, the effect is too small and

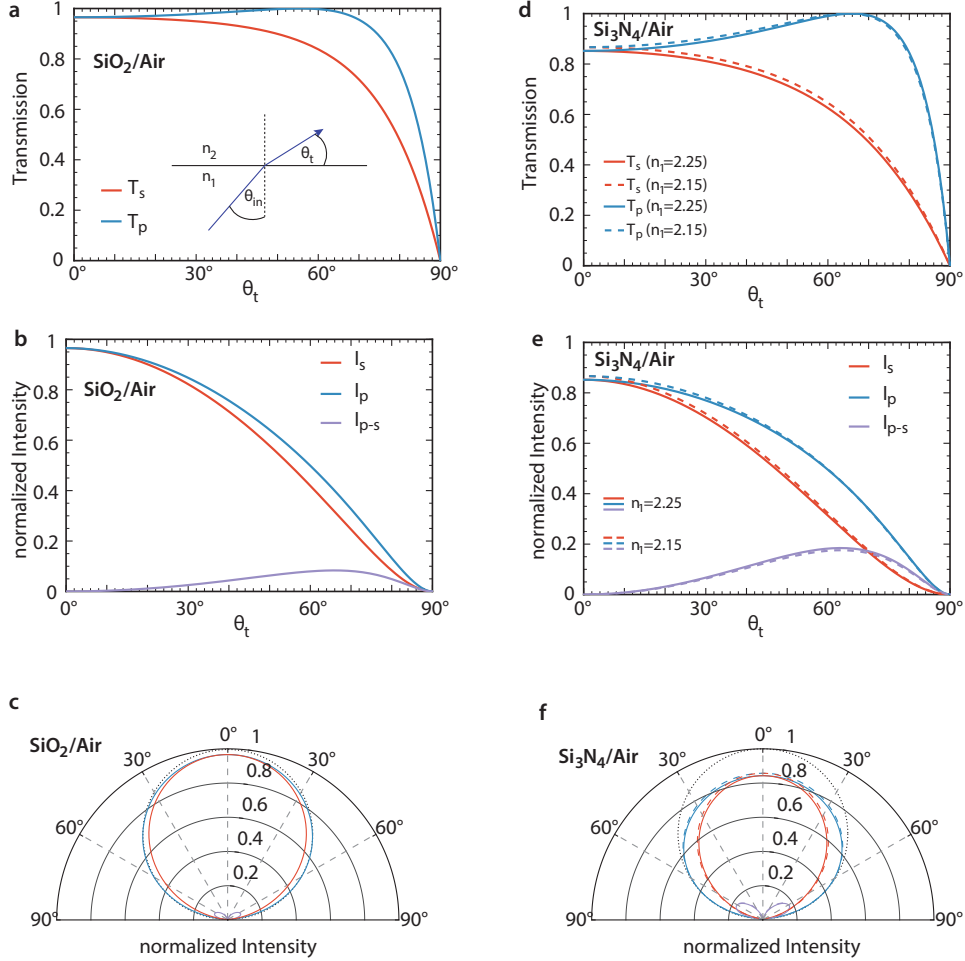


Figure A.1: The transmission coefficients of s- and p-polarized light for a silicon oxide (silicon nitride) /air interface (a,d). (b,c,e,f) Transmitted s- and p-polarized intensity (red, blue lines respectively) as normal plots (b,e) and polar plots (c,f) for both interfaces. The purple lines represent the degree of polarized emission. The intensity takes into account the Lambertian emission pattern of random radiation centers within the substrate. The black dotted line in (c,f) describes a perfect Lambertian emitter.

at the wrong angles to explain the observed polarized intensity at large angles in [Section 4.2.2](#).

A.2 Si Resonators on SiO₂ Substrate

A.2.1 Comparison of Intensity Spectra for Polarized Components

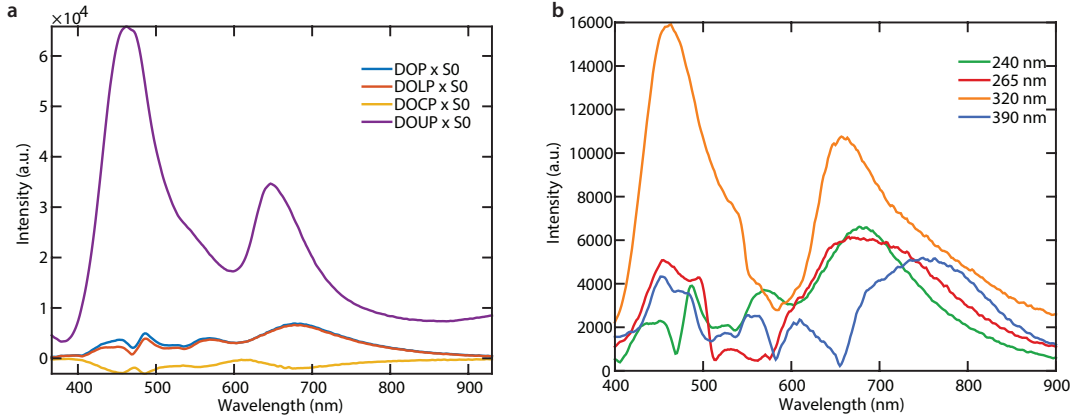


Figure A.2: (a) Product of the intensity S_0 and the different degrees of polarization plotted in [Figure 3.8a](#) for the spectral polarimetry measurement on a 240 nm resonator. (b) The product on S_0 and the $DOLP$ for measurements on resonators with different diameter (240 nm, 265 nm, 320 nm and 390 nm)

The discussion in [Section 3.3.2](#) is based on the identification of features in the $DOLP$. Since the degree of polarization is only a relative entity, the intensity spectrum $S_0(\lambda)$ needs to be taken into account if the real height of the features in [Figure 3.8](#) shall be discussed. Doing this does not lead to different outcome than that in [Section 3.3.2](#). To show this [Figure 3.8](#) displays the differently polarized intensities for a 240 nm diameter resonator (a) and the linearly polarized intensity for resonators of different sizes in (b). The same features as in [Section 3.3.2](#) can be identified and a red-shift as particle size increases can be observed. The spectral shape of S_0 has the greatest effect on the graphs at wavelengths < 420 nm since here the measured intensities fall rapidly. Additionally, peaks at the location of the strongest emission around 470 nm are increased more than the others.

A.2.2 Overview of Linearly Polarized Features in the Measured Resonators

The whole set of the measurements described in [Section 3.3.2](#) is listed in [Table A.1](#) where the linearly polarized features from polarimetry measurements on different resonators are listed. Both wavelength- and angle-resolved polarimetry measurements

were performed on all listed resonators. The results from the measurements are discussed by the representative examples in [Section 3.3.2](#).

		Central Wavelength of Bandpass Filters (nm)						
		400	450	500	550	600	650	700
Resonator Diameter (nm)	155c	420	430	-	550	620	-	-
	187c	-	-	-	550	620	-	-
	210c	-	450	-	540	600	-	-
	238c	-	-	-	-	580	-	-
	264c	-	-	490	530	610/600	-	-
	264l	-	440	-	-	-	-	-
	264r	-	440	-	-	-	-	-
	319c	426	-	525/530/560	-	-	660	-
	319r	-	465	470	544	-	-	-
	392c	400	-	520/520	550/550/570	610	-	680
	392l	400	-	-	-	-	-	-
	392r	400	-	-	-	-	-	-
	482c	400	-	511	540	611	-	-
	482r	400	450	-	-	611	-	680

Table A.1: The identified features in spectral and angular polarimetry measurements for resonators of different diameters (rows). The found candidates are sorted according to the available bandpass filters for angular measurements (columns) and their central wavelengths are listed in the table. The labels c, l and r of the resonator diameters indicate excitation in the center, at the left or at the right edge respectively. Features with bold printed wavelengths were found in both experiment and FDTD simulations. Italic numbers indicate weakly pronounced features. Blue printed wavelengths were identified in spatial 2D plots of the DOLP, the rest results from spatially averaged spectra of the DOLP (smaller particles). No full angular polarimetry measurements are available for cells with a red background.

A.2.3 Linearly Polarized Intensity in Angular Measurements

[Figure A.3](#) shows complementary information to [Figure 3.9](#), taking into account the total emitted intensity S_0 . The observations are consistent with the discussed features in [Section 3.3.2](#).

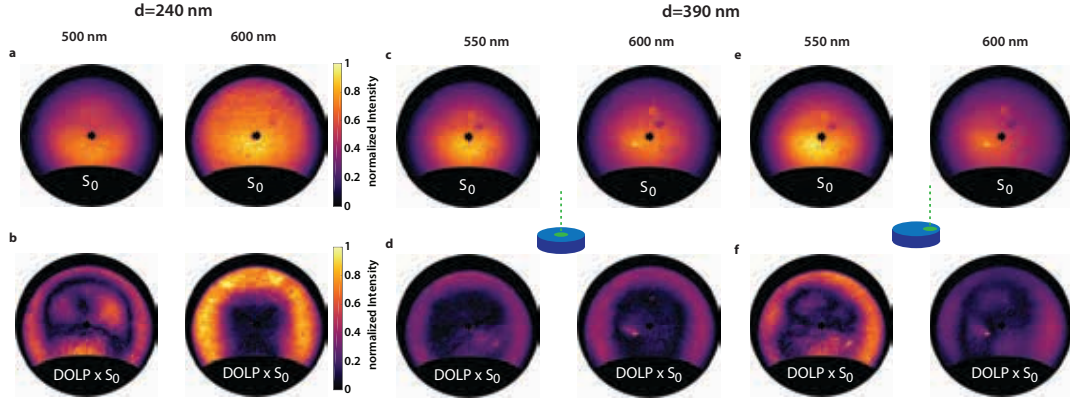


Figure A.3: Top row: Total intensity S_0 of the two resonators investigated in [Section 3.3.2](#) at the discussed wavelengths. Bottom row: Linearly polarized intensity $DOLP \times S_0$ for both resonators at the same wavelengths. (e,f) plot the data from measurements with excitation at the edge of a particle. All plots are normalized to the maximum intensity.

A.3 Si Resonators on Si_3N_4 Substrate

A.3.1 Linearly Polarized Intensity and Total Intensity in Spectral Measurements

To take the spectral shape of the total intensity into account and to get information about the energy distribution in the different polarized features the Stokes parameter S_0 (total intensity) and the linearly polarized intensity ($DOLP \times S_0$) are plotted in [Figure A.4](#) correspondingly to [Figure 4.5](#).

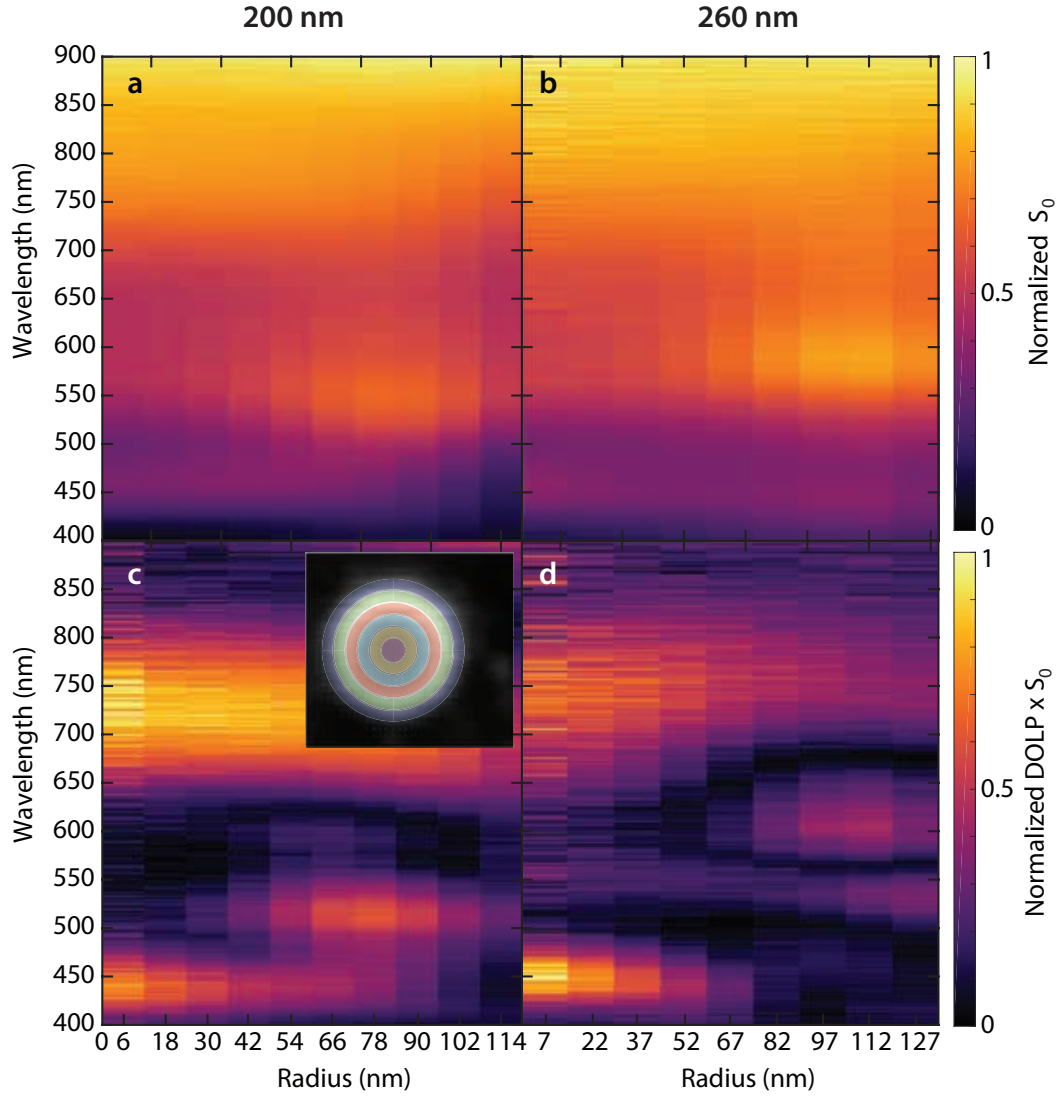


Figure A.4: The total emitted intensity ($S_0 = I_{hor} + I_{ver}$) for the 200 nm (a) and 260 nm (b) diameter resonators and the linearly polarized emitted intensity for both resonators (c,d).

A.3.2 Degree of Circularly Polarization

Figure A.5 displays the DOCP detected at the discussed wavelengths of the 200 nm diameter and 260 nm diameter particle measured at both excitation positions. In all cases the DOCP is relatively small in amplitude and thus matches the expectations. The patterns for symmetric excitation resemble expected effects from the paraboloidal mirror and an insufficient correction. The asymmetric excitation breaks the pattern. However, no directional features are present, which could indicate emission from resonant modes.

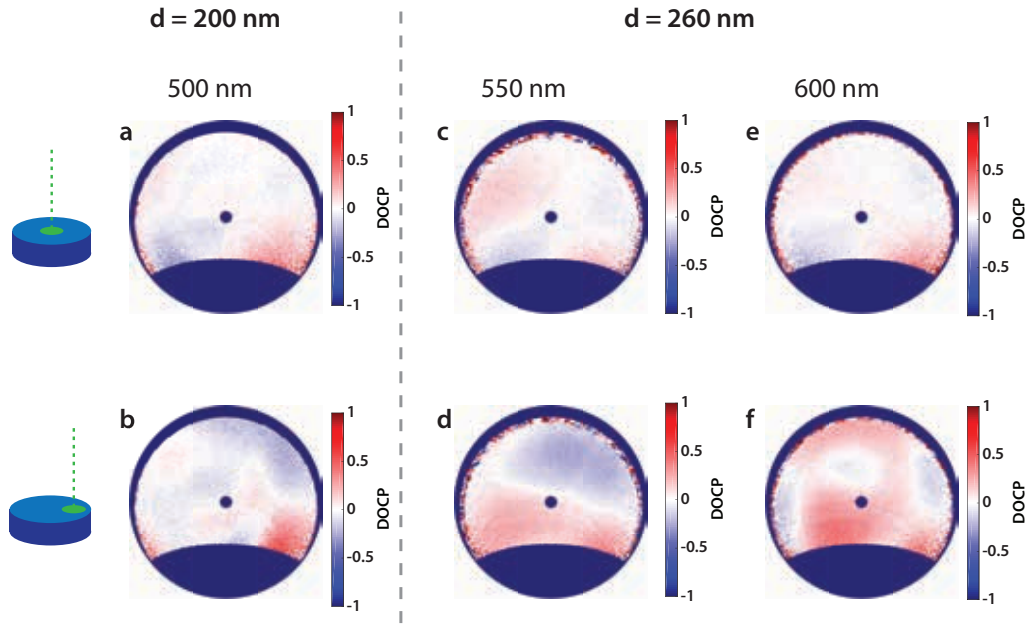


Figure A.5: The degree of circularly polarized light corresponding to the data shown in Figure 4.6.

A.3.3 Linearly Polarized Intensity in Angular Measurements

For a better comparison of measurement results (Figure 4.6) and simulation (Figure 4.9) the intensity of the linearly polarized light is plotted in Figure A.6. It is the product of the measured $DOLP$ and the total intensity S_0 . The 600 nm emission pattern of the centrally excited 260 nm diameter particle exhibits some similarities to a combination of modes measured in previous studies [16]. Compared to the $DOLP$ in Figure 4.6, the features in the center of the plot are more pronounced in addition to weaker features at grazing angles. This corresponds to the general trend of $DOLP$ (low in center, high at large θ) and S_0 (concentrated around center) in Figure 4.6. However, the high intensity feature at large θ is still dominant (Figure A.6a,b,e) and

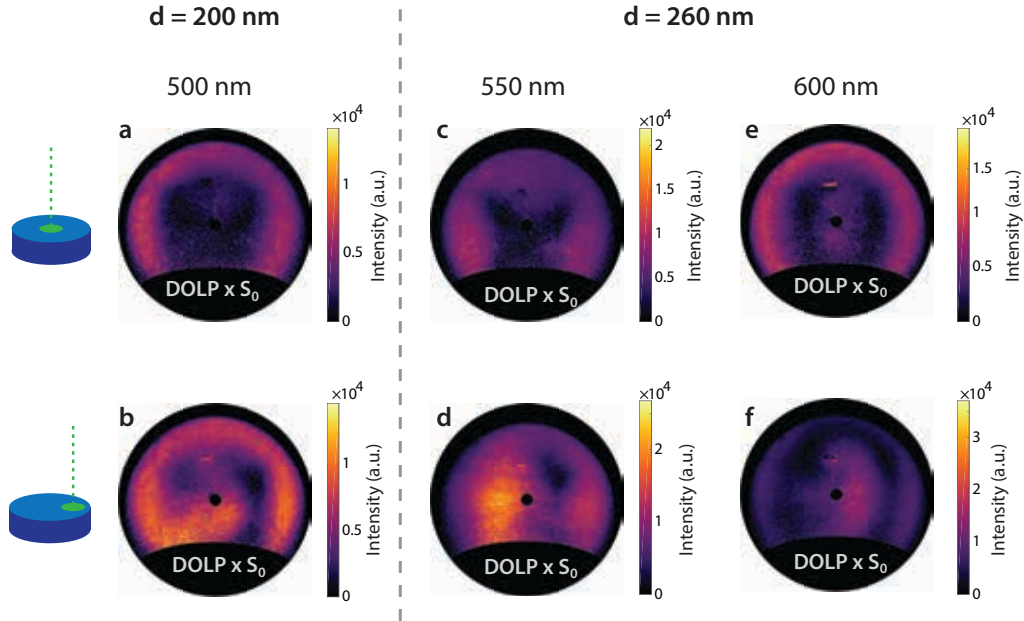


Figure A.6: The linearly polarized part of light emitted at 500 nm for the smaller 200 nm diameter resonator (a,b) and at 550 nm and 600 nm for the 260 nm diameter resonator (c-f). The top row displays the result from measurements with central excitation and the bottom row those from edge excitation.

located at angles which are larger than those expected from other effects such as transition radiation [25].

A.4 Sample Destruction by Electron-Beam Irradiation

The angle resolved polarimetry measurements in [Section 3.3.2](#) and [Section 4.2.2](#) lead to long exposure times of the sample since one polarimetry measurement consists of six individual polarization measurements plus one total intensity measurement each about 1 min long. During these measurement the electron beam is positioned on the same spot on the sample. Since each measurement requires a pre-irradiation step to stabilize the background radiation it is preferable to perform multiple measurements on the same structure which enables a better comparison as well. However, a non trivial effect of the electron-beam on the sample could be observed at the chosen beam and measurement parameters which leads to destruction of the sample during the measurement. [Figure A.7](#) shows the influence of the electron-beam in SEM images taken before and after angular CL measurements. The two excitation positions in the center and at the edge are clearly visible in [Figure A.7d,f](#). Due to this effect, not more than three to four angular polarimetry measurements were performed on the

same resonator.

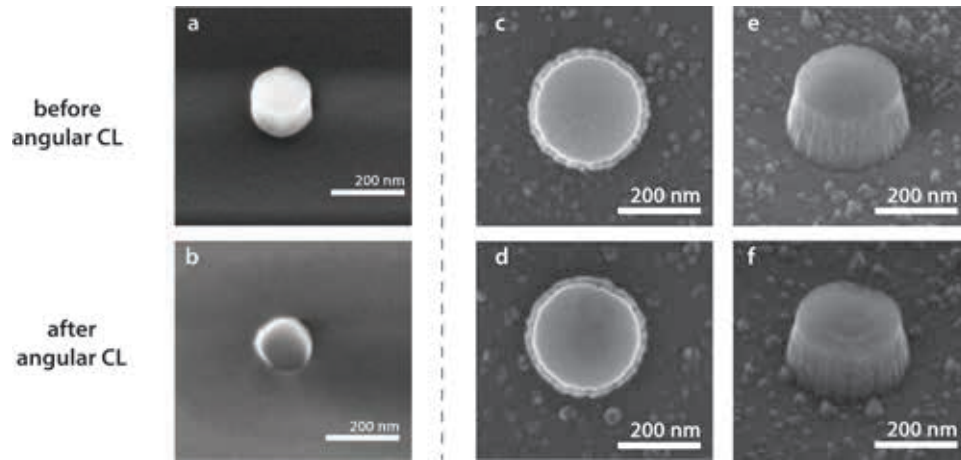


Figure A.7: Effect of the electron-beam on the sample during angular measurements. Figures (a) and (b) show a particle on the silicon dioxide based sample before and after five subsequent CL polarimetry measurements. Figures (c) and (e) show a particle on the silicon nitride based sample before, figures (d) and (f) a particle of the same size after three angular polarimetry measurements.

Acknowledgements

Even though it is only a Master's project, the conducted research described in this thesis required a large amount of work which cannot possibly be attributed to a single person. Thus, I want to mention a selection of those who were actively or passively involved in the achievements of this study. First of all, I thank Albert Polman, who is outstanding person in promoting innovative, high potential but risky research topics. Without him, this study - less risky but still far away from trivial - would have never been possible. The same holds for Benjamin Brenny, aka the CL-Guru. Without his inexhaustible knowledge (and his inexhaustible ability to distribute knowledge) about everything around cathodoluminescence I would have had a bad time in getting to know AMOLF and the experiment and in interpreting my measurements. Next, Mark Knight played a key role in organizing the scientific exchange and was always a great resource of general and specialized advice. A different, but not less helpful perspective was often provided by Sophie Meuret who enriched the work at AMOLF when she joined the group after about half of the time of this project. Another kind of support came from the other Master students in the Photonic's Materials group. The fact that we all had to overcome the same obstacles finding our way into research lead to great discussions, jokes and knowledge exchange. Having Philipp Tockhorn, Theresa Ortmann and Verena Neder by my side has made my Master's project even more unique. Finishing the list of AMOLF medewerkers, I shall not forget to acknowledge the highly motivated support from the cleanroom and microscopy team, comprising Hans Zeijlemaker, Andries Lof and Dimitry Lamers.

The second group of people I want to thank contains all the friends I have been in contact with, and who were in similar situations than mine. Here I need to name my very special flatmates, Benni, Angeliki and Verena which made it possible to spend a year living in surroundings characterized by laughter and harmony. Especially Verena, who has been working next door to me and who is responsible that I had lunch with me at no less than 70% of the days, earns to be mentioned repetitively at this point. Also, I want to thank all those who were close to me. And lastly, special thanks goes to my family for the endless support and for making it possible for me to pursuing a Master's degree in physics in Amsterdam. This list is far from any claim of completeness and there are many others who contributed to this recent achievement of mine and I am grateful to know every single one of them.